

RESEARCH ARTICLE

SPECIAL ISSUE: CELL BIOLOGY OF LIPIDS

Snazarus and its human ortholog SNX25 modulate autophagic flux

Annie Lauzier¹, Marie-France Bossanyi¹, Raphaëlle Larcher¹, Sonya Nassari¹, Rupali Ugrankar², W. Mike Henne² and Steve Jean^{1,*}

ABSTRACT

Macroautophagy, the degradation and recycling of cytosolic components in the lysosome, is an important cellular mechanism. It is a membrane-mediated process that is linked to vesicular trafficking events. The sorting nexin (SNX) protein family controls the sorting of a large array of cargoes, and various SNXs impact autophagy. To improve our understanding of their functions *in vivo*, we screened all *Drosophila* SNXs using inducible RNA interference in the fat body. Significantly, depletion of Snazarus (Snz) led to decreased autophagic flux. Interestingly, we observed altered distribution of Vamp7-positive vesicles with Snz depletion, and the roles of Snz were conserved in human cells. SNX25, the closest human ortholog to Snz, regulates both VAMP8 endocytosis and lipid metabolism. Through knockout-rescue experiments, we demonstrate that these activities are dependent on specific SNX25 domains and that the autophagic defects seen upon SNX25 loss can be rescued by ethanolamine addition. We also demonstrate the presence of differentially spliced forms of SNX14 and SNX25 in cancer cells. This work identifies a conserved role for Snz/SNX25 as a regulator of autophagic flux and reveals differential isoform expression between paralogs.

KEY WORDS: Snazarus, Sorting nexin 25, Autophagy, VAMP8, Endocytosis, Trafficking, Lipid metabolism

INTRODUCTION

Macroautophagy, hereafter termed autophagy, is a crucial homeostatic and stress-responsive catabolic mechanism (Doherty and Baehrecke, 2018; Mizushima et al., 2008). Autophagy is characterized by the formation of double-membrane structures, called phagophores, which expand and incorporate cytoplasmic proteins or organelles (Gatica et al., 2018; Mizushima et al., 2011). These structures ultimately close to form autophagosomes (Reggiori and Ungermann, 2017). When mature, the autophagosomes fuse with lysosomes, and autophagosomal content is degraded by lysosomal enzymes and recycled (Kriegenburg et al., 2018; Lőrincz and Juhász, 2019; Nakamura and Yoshimori, 2017). Hence, autophagy requires an intricate balance between various cellular processes to ensure appropriate cargo selection, and autophagosome formation, maturation and fusion (Levine and Kroemer, 2019).

Although the core signaling pathways controlling autophagy induction in response to stress were rapidly described and are now well understood (Harder et al., 2014; Korolchuk et al., 2011; Lamb et al., 2013), the molecular mechanisms controlling autophagosome sealing, maturation and fusion were only defined more recently (Lőrincz and Juhász, 2019). Findings in yeast and metazoans have shed light on the molecular machinery required for autophagosome-lysosome fusion and its regulation. Although different proteins are involved in autophagosome-vacuole fusion in yeast and autophagosome-lysosome fusion in metazoans (Reggiori and Ungermann, 2017), the overarching principle is conserved and requires the presence of specific soluble N-ethylmaleimide-sensitive factor attachment receptors (SNAREs) (Itakura et al., 2012; Lőrincz and Juhász, 2019; Nakamura and Yoshimori, 2017). In metazoans, syntaxin (STX)17 is recruited to mature autophagosomes by two hairpin regions, where it forms a Qabc complex with synaptosome associated protein 29 (SNAP29) (Itakura et al., 2012; Takáts et al., 2013). The STX17–SNAP29 complex then forms a fusion-competent complex with lysosome-localized vesicle associated membrane protein (VAMP)8 (Itakura et al., 2012). More recently, the Qa SNARE YKT6 v-SNARE homolog (YKT6) was also found to mediate autophagosome-lysosome fusion (Bas et al., 2018; Matsui et al., 2018; Takáts et al., 2018). YKT6 is recruited to mature autophagosomes and associates with SNAP29. The YKT6–SNAP29 complex interacts with the lysosomal R-SNARE STX7 to mediate fusion (Bas et al., 2018; Matsui et al., 2018; Takáts et al., 2018). These fusion complexes are conserved, and flies also use these proteins for autophagosome-lysosome fusion (Takáts et al., 2013, 2018). However, unlike in human cells, where STX17 and YKT6 act redundantly in parallel pathways, *Ykt6* is epistatic to *Syx17* and *Vamp7* in flies (Takáts et al., 2018). SNARE functions are supported by other intracellular factors, which ensure their specificity and rapid action (Bröcker et al., 2010; Hong, 2005). The small Rab GTPases Ras-related protein (RAB)7 and RAB2 are important determinants of fusion (Baba et al., 2019; Fujita et al., 2017; Hegedűs et al., 2016; Kuchitsu et al., 2018; Lőrincz et al., 2017b; Wang et al., 2016), as lysosome-localized RAB7 and autophagosome-localized RAB2 interact with the tethering homotypic fusion and vacuole protein sorting (HOPS) complex to bring autophagosomes and lysosomes in close proximity and enable SNARE-mediated fusion (Fujita et al., 2017; Lőrincz et al., 2017b; Numrich and Ungermann, 2014). Interestingly, a direct interaction has been observed between STX17 and the HOPS complex (Jiang et al., 2014; Takáts et al., 2014), favoring autophagosome-lysosome tethering. The lipid composition of autophagosomes and lysosomes is also an important determinant of fusion. Specific phosphoinositides [PtdIns(3)P, PtdIns(3,5)P₂, PtdIns(4)P, and PtdIns(4,5)P₂] impact fusion through different mechanisms (Lőrincz and Juhász, 2019). Low cholesterol levels affect autophagosome tethering to late endosomes/lysosomes (Wijdeven et al., 2016), while increased

¹Faculté de Médecine et des Sciences de la Santé, Département d'immunologie et de biologie cellulaire, Université de Sherbrooke, 3201, Rue Jean Mignault, Sherbrooke, Québec, Canada J1E 4K8. ²Department of Cell Biology, UT Southwestern Medical Center, 6000 Harty Lines Boulevard, Dallas, TX 75390, USA.

*Author for correspondence (steve.jean@usherbrooke.ca)

DOI: 10.1242/jcs.258733

Handling Editor: James Olzmann
Received 8 April 2021; Accepted 12 November 2021

saturated fatty acid levels or a high-fat diet in mice decrease fusion events (Koga et al., 2010; Miyagawa et al., 2016). Recently, the phosphatidylserine:phosphatidylethanolamine ratio was also demonstrated to affect autophagosome-lysosome fusion (Ma et al., 2018).

It is clear that multiple inputs are integrated to regulate the final step of the autophagic process. Accordingly, trafficking events must properly regulate the trafficking of essential SNAREs involved in autophagosome-lysosome fusion, like VAMP8 and STX7, that also mediate various other membrane fusion events (Cornick et al., 2019; Diaz-Vera et al., 2017; Jean et al., 2015; Nair-Gupta et al., 2014; Okayama et al., 2009; Pattu et al., 2011; Zhu et al., 2012). This is also true for the dynamic regulation of the lipid composition of these organelles, given that inappropriate ratios of specific lipids affect autophagic flux (Lőrincz and Juhász, 2019). Hence, defining trafficking regulators coordinating the localization of SNAREs, as well as the lipid composition of autophagosomes and lysosomes, is of paramount importance for better understanding of the dynamic link between trafficking and autophagy.

One class of endosomal sorting regulators is the sorting nexin (SNX) family (Chi et al., 2015; Cullen, 2008; van Weering and Cullen, 2014). These proteins have phox homology (PX) domains that interact with diverse phosphoinositide species (Chandra et al., 2019). Many SNXs localize to early endosomes, where they are involved in sorting events (Cullen, 2008). Importantly, a few SNXs play roles in autophagy (Knævelsrud et al., 2013; Maruzs et al., 2015). SNX18 and SNX4–SNX7 heterodimers control autophagy-related (ATG)9 trafficking to modulate autophagosome expansion (Antón et al., 2020; Knævelsrud et al., 2013; Ravussin et al., 2021), and SNX5 and SNX6 also indirectly regulate autophagy by modulating cation-independent mannose-6-phosphate receptor sorting, affecting lysosomal functions (Cui et al., 2019). In yeast, SNX4 regulates autophagosome-lysosome fusion by controlling endosomal phosphatidylserine levels (Ma et al., 2018). These reports highlight the multifaceted roles of SNXs in regulating autophagy. However, SNX involvement in SNARE protein trafficking has not been reported.

Here, using *Drosophila* as a simple system to screen genes involved in autophagy, we have identified the sorting nexin Snazarus (Snz) and its human ortholog SNX25 as regulators of the localization and lipid metabolism of Vamp7 and VAMP8, respectively. Using RNA interference (RNAi) and clustered regularly interspaced short palindromic repeats (CRISPR)/Cas9-generated mutants, as well as ethanolamine supplementation, we show that loss of Snz decreases autophagic flux. Importantly, we show that this effect is independent of the endoplasmic reticulum (ER) localization of SNX25 and that it affects two independent processes – Vamp7/VAMP8 internalization and lipid homeostasis. Altogether, these findings identify Snz and SNX25 as regulators of autophagic flux.

RESULTS

snz is required for autophagic flux

To identify SNXs involved in autophagy, we used the *Drosophila* fat body as an inducible system to monitor autophagy *in vivo*. Although SNXs have been previously screened for functions in autophagy, these screens monitored Atg8 and focused on SNXs that decreased autophagosome formation (Knævelsrud et al., 2013; Mauvezin et al., 2016). Thus, to identify SNXs that may have been missed because of gene redundancy or weak effects on Atg8, we focused on the terminal stages of autophagy by monitoring autolysosome acidification using LysoTracker (LyTr) staining of

third-instar fat bodies from starved larvae. Autophagy is developmentally regulated in the fat body (Rusten et al., 2004; Scott et al., 2004) and acidified organelles are not present in fed third-instar larvae. However, upon starvation of third-instar larvae, autophagy is induced, and acidified organelles can be detected by LyTr staining. This specific property of the fat body has been widely used to assess the terminal steps of autophagy (Lőrincz et al., 2017a; Mauvezin et al., 2014), given that lysosomal acidification solely occurs in autophagy-proficient cells in this organ (Mauvezin et al., 2014). Using RNAi, we depleted individual SNXs from starved fat bodies and counted the LyTr puncta detected through automated image analysis (Fig. 1A,B). As previously demonstrated, we observed effects for SNX18 (Knævelsrud et al., 2013; Sørensen et al., 2018) and most retromer-associated SNXs (Cui et al., 2019), illustrated by significant reductions in LyTr puncta in cells depleted of them (Fig. 1A,B). Interestingly, we observed a strong reduction in the number of LyTr puncta in fat bodies depleted of Snz (Suh et al., 2008; Ugrankar et al., 2019) (Fig. 1A,B). This SNX has four orthologs in humans, SNX13, SNX14, SNX19 and SNX25 (Henne et al., 2015; Ugrankar et al., 2019). Snz and SNX14 have both been shown to be anchored to the ER, and to mediate lipid droplet (LD) formation in flies and human cells, respectively (Bryant et al., 2018; Datta et al., 2019; Ugrankar et al., 2019). Moreover, recent findings have demonstrated a role for SNX14 in regulating saturated fatty acid metabolism (Datta et al., 2020). Given the strong decrease in autolysosome acidification in *snz*-depleted cells, and the fact that autophagy and lipid metabolism are intimately linked (Koga et al., 2010; Rambold et al., 2015; Velázquez et al., 2016), we examined a potential role for Snz in regulating autophagy.

We first analyzed autophagic flux by monitoring ref(2)P, the fly ortholog of p62 (p62 is also known as SQSTM1) (Devorkin and Gorski, 2014). Ref(2)P is an autophagic substrate that is engulfed by autophagosomes and degraded after fusion. Hence, its accumulation suggests defective autophagic flux (Devorkin and Gorski, 2014). Using a validated *snz* RNAi line (Ugrankar et al., 2019) with efficient depletion of ectopically expressed Snz:GFP (Fig. S1A), we observed increased ref(2)P puncta in Snz-depleted fat bodies compared to controls (Fig. 1C,D). This finding was independently corroborated by western blot analysis (Fig. 1E). To more directly assess autophagic flux, we used the green fluorescent protein (GFP):mCherry:Atg8 reporter. This probe allows differentiation between autophagosomes (yellow) and autolysosomes (red), since the fluorescence from GFP is quenched at the acidic pH of the lysosome (Mauvezin et al., 2014). Consistent with the ref(2)P results, we observed an accumulation of autophagosomes (yellow objects) in Snz-depleted fat bodies compared to what was seen in control fat bodies (Fig. 1C,F). To further corroborate these RNAi findings, we used a CRISPR/Cas9-generated deletion of *snz* (Ugrankar et al., 2019). In mutant animals, we observed decreased LyTr puncta (Fig. 1G,H) and autophagosome accumulation (Fig. 1G,I), albeit to a lower extent than with RNAi, potentially due to genetic compensation in the mutant as frequently observed between full mutants and RNAi-mediated knockdowns (El-Brolosy and Stainier, 2017). Given its requirement for full autophagic flux, we tested whether Snz overexpression could drive or potentiate autophagy. Fat bodies overexpressing a Snz:GFP transgene (Ugrankar et al., 2019) did not show an increased abundance of autolysosomes under either fed or starved conditions (Fig. S1B,C). By contrast, a significant decrease in LyTr puncta was observed after a 3-h starvation period (Fig. S1B,C). We conclude from these results that Snz is necessary but not sufficient for autophagic flux.

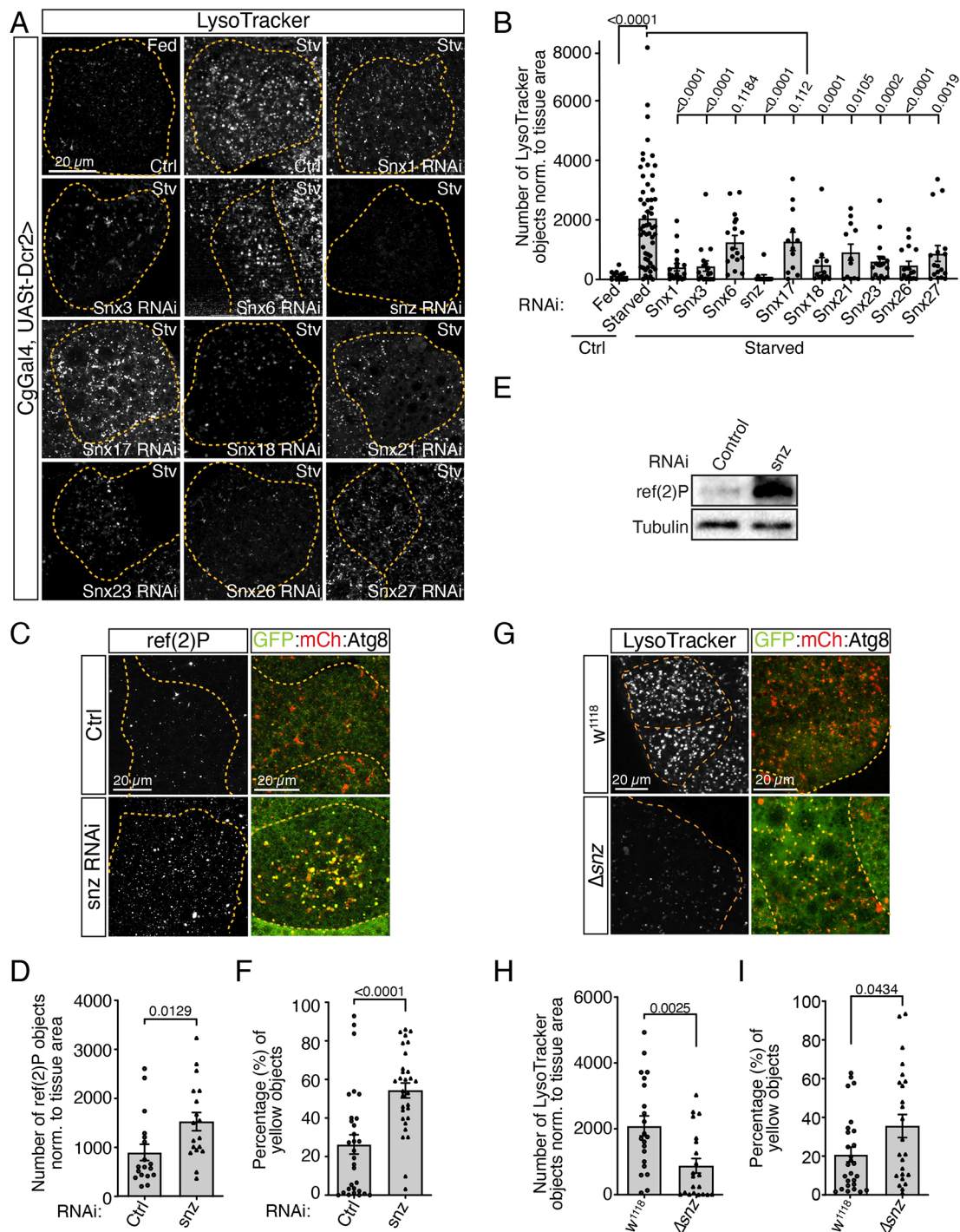


Fig. 1. Snz is required for full autophagic flux in the *Drosophila* fat body. Results are from LyTr (LysoTracker) staining of fed and starved (3 h) third-instar *Drosophila* larvae fat bodies. (A) Representative LyTr images of starved fat bodies depleted of all individual SNXs by RNAi. Orange dotted lines indicate individual cells. (B) Mean LyTr-positive puncta normalized to the tissue area. Bars represent the mean, individual points represent single fat body values, and the error bars are the s.e.m. ($n \geq 2$ independent experiments). Autophagy was assessed in fed and starved (3 h) third-instar *Drosophila* fat bodies. (C) Ref(2)P-positive puncta (fed) and GFP:mCh:Atg8 colocalization (starved 3 h) in Snz-depleted and control fat bodies. Orange dotted lines indicate individual cells. (D) Number of ref(2)P-positive puncta normalized to the tissue area. Bars represent the mean, individual points or triangles represent single fat body values, and the error bars are the s.e.m. ($n = 3$ independent experiments). (E) Ref(2)P protein levels in third-instar fat body extracts in the presence and absence of Snz RNAi. Immunoblots are representative of three independent experiments. (F) Percentage of autophagosomes (yellow objects) per image. Bars represent the mean, individual points or triangles represent single fat body values, and the error bars are the s.e.m. ($n = 4$ independent experiments). (G) LyTr-positive puncta and GFP:mCh:Atg8 colocalization in snz-mutant and parental (*W¹¹¹⁸*) starved (3 h) fat bodies. Orange dotted lines indicate individual cells. (H) Number of LyTr-positive puncta normalized to the tissue area. Bars represent the mean, individual points or triangles represent single fat body values, and the error bars are the s.e.m. ($n = 4$ independent experiments). (I) Percentage of autophagosomes (yellow objects) per image. Bars represent the mean, individual points or triangles represent single fat body values, and the error bars are the s.e.m. ($n = 4$ independent experiments). *P*-values calculated as described in the Materials and Methods are shown.

The autophagic roles of Snz are conserved in mammals

snz has four orthologs in mammals, including *SNX14*, a gene mutated in spinocerebellar ataxia autosomal recessive 20 (SCAR20), which can influence autophagy by impacting lysosomal function (Akizu et al., 2015). Sequence alignments indicate that the closest ortholog of *snz* is *SNX25*, and the Snz PX domain shows an *SNX25*-like affinity for di-phosphoinositides, rather than the lack of binding specificity displayed by *SNX14* (Chandra et al., 2019) or the PtdIns(3)P specificity of *SNX19* (Saric et al., 2021). To test for functional conservation, we depleted *SNX13*, *SNX14* and *SNX25*, which have similar domain organizations to Snz, in HeLa cells using two independent small interfering (si)RNAs per gene (Fig. 2A). Analysis of the amount of the lipidated form of microtubule associated protein 1 light chain 3 proteins (LC3), LC3-II, from cells in full medium revealed increases in *SNX14*- and *SNX25*-depleted cells, although these were not statistically significant (Fig. 2B,C). Higher LC3-II levels suggest either increased autophagosome synthesis or defective autophagosome degradation. To assess this, we treated depleted cells with bafilomycin A1 (BafA1) to block autophagosome degradation. In BafA1-treated cells, no increase in LC3-II was observed after *SNX* depletion compared to control cells (Fig. 2B). Given the variability in the western blot analysis, endogenous LC3 levels were assessed in depleted cells by immunofluorescence. Depletion of *SNX14* and *SNX25* led to statistically significant increases in the number of LC3 puncta per cell, and no further increase was observed after BafA1 treatment (Fig. 2D,E). As a recent report revealed that *SNX19* mediates ER-endolysosome contact sites (Saric et al., 2021), we tested the impact of its depletion on autophagy. Using two siRNAs targeting *SNX19* (Fig. S1D), we did not observe strong LC3-II accumulation by western blot (Fig. S1E) or immunofluorescence analysis (Fig. S1F,G). If anything, a slight decrease was observed in *SNX19*-depleted cells in normal growth conditions (Fig. S1F,G). These data suggest impaired autophagic flux in cells depleted of *SNX14* and *SNX25*, while *SNX13* and *SNX19* did not show strong effects. Given the phenotypes observed in *SNX14* and *SNX25* siRNA-transfected cells, we next generated *SNX14* and *SNX25* single and double knockout (KO) populations using CRISPR/Cas9-based gene editing. Statistically significant increases in LC3-II were observed in independently generated KO populations (Fig. 2F,G), and further confirmed by measuring of LC3 immunofluorescence in *SNX25* KO cells (see Figs 6 and 7). Altogether, these results indicate positive roles for *SNX14* and *SNX25* in controlling autophagic flux. They are consistent with the observed effect of Snz depletion in the fly fat body and in agreement with findings from patients with SCAR20 (Akizu et al., 2015).

General trafficking pathways are not affected by *SNX14*, *SNX25* or Snz depletion

To determine which cellular processes were impacted by *SNX14* and *SNX25* depletion, we first monitored lysosomal functions. Lysosomal cathepsin B activity was assessed using Magic Red, which emits fluorescence only when cleaved by active cathepsin B (Mauvezin et al., 2014). HeLa cells depleted for each Snz ortholog by siRNA were imaged live using widefield fluorescence microscopy, and the average number of Magic Red puncta was measured in each cell and experiment. A non-significant decrease was observed after *SNX14* depletion, while no clear variations were observed in *SNX13*- or *SNX25*-depleted cells, suggesting that cathepsin B activity was not impaired (Fig. S2A,B). We also assessed epidermal growth factor receptor (EGFR) degradation in KO cells as an indicator of lysosomal function. As expected, EGF stimulation led to potent extracellular-regulated kinase (ERK1/2)

activation and resulted in EGFR degradation in all conditions (Tan et al., 2015), with similar kinetics between control and *SNX14*/*SNX25* single KOs (Fig. S2C,D). Co-ablation of *SNX14* and *SNX25* led to a slight delay in EGFR degradation. Notably, there were no obvious differences in the localization, intensity and number of early endosome antigen 1 (EEA1), APPL1- and CD63-positive compartments (Fig. S2E). From these results, we conclude that *SNX13*, *SNX14* and *SNX25* can compensate for each other and that their individual loss does not affect lysosomal function; however, co-depletion of *SNX14* and *SNX25* impairs either lysosomal function or EGFR trafficking to the lysosomes to some degree.

Given the partial redundancy observed between *SNX14* and *SNX25* with regard to lysosomal function, we tested the impact of depleting Snz, their lone *SNX* ortholog in flies. RNAi depletion of Snz from the fat body did not significantly impact early endosomes, late endosomes or lysosomes (indicated by Rab5, Rab7 and Lamp1, respectively; Fig. 3A–D). Importantly, both the number and shape of these compartments were similar between control and Snz-depleted cells. We also tested lysosomal functions in fly macrophages (hemocytes), which have constitutive lysosomal functions, unlike the fat body. LyTr staining and cathepsin B activity did not decrease in the hemocytes of *snz*-ablated flies; on the contrary, increased LyTr- and Magic Red-positive compartments were observed (Fig. 3E–G). Taken together, data obtained from HeLa cells and *Drosophila* indicate that loss of Snz or its mammalian orthologs *SNX14* and *SNX25* impairs autophagic flux, without potentially impairing general endolysosomal compartments.

Vamp7/VAMP8 trafficking is perturbed in Snz/*SNX25*-depleted cells

SNARE proteins are essential regulators of autophagic flux (Moreau et al., 2011; Nair et al., 2011), and their trafficking must be regulated to account for increased autophagic demands (Jean et al., 2015). Previous studies have reported trafficking defects for small R-SNAREs that impair autophagy without obvious lysosomal effects (Jean et al., 2015; Moreau et al., 2014). Hence, we assessed the localization of GFP-tagged Vamp7, the single *Drosophila* ortholog of mammalian VAMP7 and VAMP8, in fly fat bodies (Jean et al., 2015; Takáts et al., 2013). In control cells, GFP:Vamp7 was observed in plasma membrane (PM) invaginations and in some small intracellular puncta (Fig. 3H). In Snz-depleted cells, aberrant intracellular GFP:Vamp7 puncta were abundant (Fig. 3H and I, labeled by blue arrowheads in H). Moreover, GFP:Vamp7 aggregates were observed in close proximity to the PM in various fat body cells (Fig. 3H, red arrows on the top confocal section and highlighted in the magnified inset). These observations suggest a potential role for Snz in modulating Vamp7 internalization or trafficking. To further corroborate these findings, we focused on *SNX25*, the closest ortholog to Snz, and assessed VAMP8 localization in starved *SNX25*-KO HeLa cells. Similar to our observations in flies, VAMP8 accumulated at the PM and displayed reduced colocalization with CD63, a late endosomal protein (Fig. 3J,K). Altogether, these results indicate a conserved role for Snz and *SNX25* in regulating the trafficking or endocytosis of fly Vamp7 and human VAMP8, respectively.

Snz and *SNX25* colocalize with Vamp7 and VAMP8, respectively

To further examine the link between Snz/*SNX25* and Vamp7/VAMP8, we performed colocalization studies. It is worth noting that the PX domains of both Snz and *SNX25* have affinity for di-phosphorylated phosphoinositides, including PtdIns(4,5)P₂,

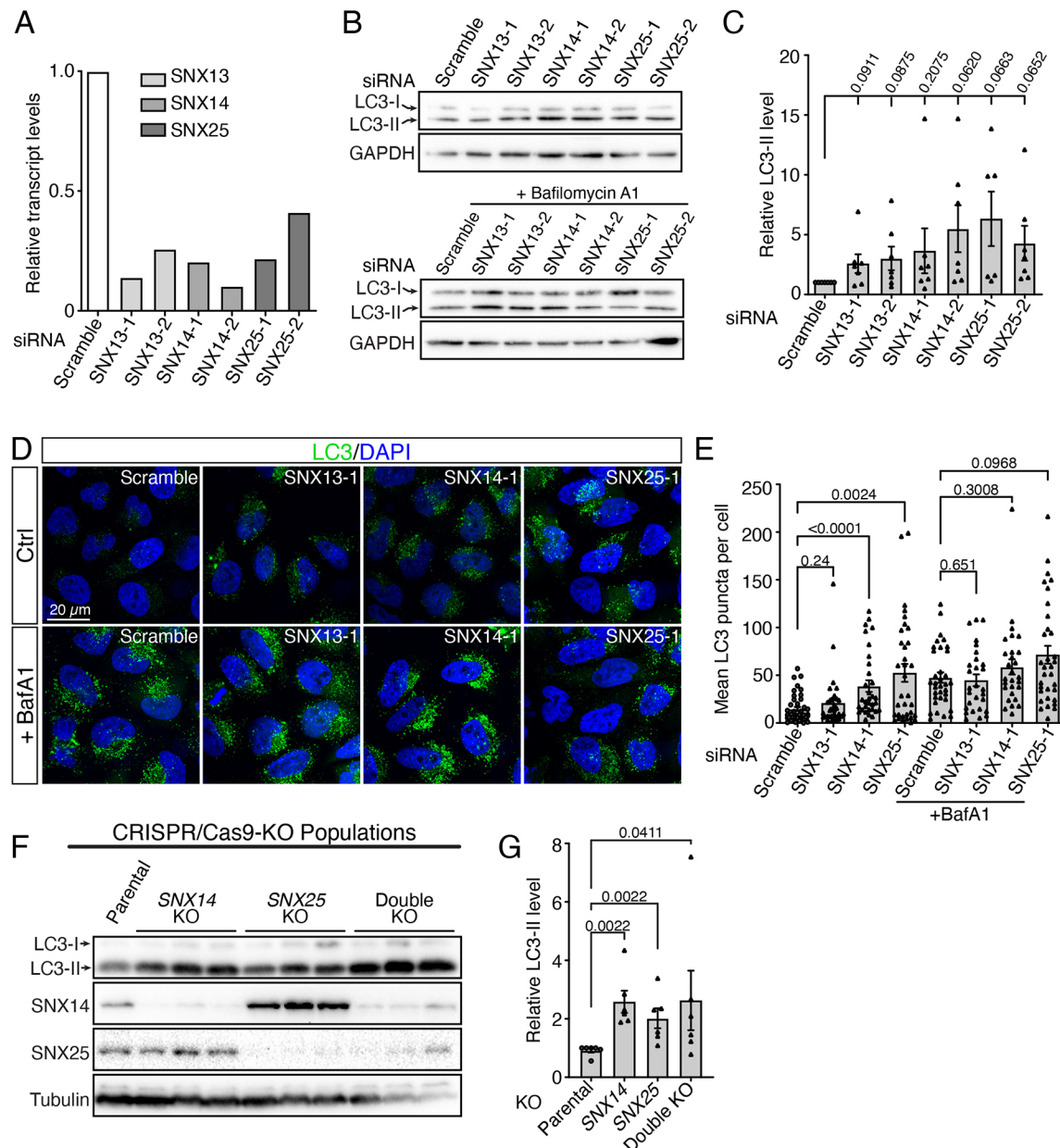


Fig. 2. Snz orthologs positively regulate autophagic flux in HeLa cells. (A) qRT-PCR validation of siRNA efficiencies. Individual controls were performed for each gene knockdown, but for ease of representation, only a single scramble control is shown. All reactions were normalized to their respective controls, which were set at 1. (B) Anti-LC3 western blots of SNX13, SNX14 and SNX25 siRNA-transfected HeLa cells grown in complete DMEM treated with or without BafA1. GAPDH was used as a loading control. (C) LC3-II/GAPDH ratios in $n > 5$ independent experiments. Bars represent the mean, individual points or triangles represent single experimental values, and the error bars are the s.e.m. (D) Immunofluorescence analysis of endogenous LC3 (green) in HeLa cells grown in complete DMEM with or without BafA1 treatment. Nuclei were counterstained with DAPI. Images are representative of three independent experiments. (E) Quantification of LC3 puncta per cell. Bars represent the mean, individual points or triangles represent single-cell values, and the error bars are the s.e.m. ($n = 3$ independent experiments). (F) Western blots of CRISPR/Cas9-generated independent SNX14, SNX25 and double SNX14 and SNX25 KO cell populations in normal growth conditions. (G) Quantification of LC3-II levels (normalized to tubulin) in SNX14, SNX25 and double SNX14/SNX25 KO cell populations. Bars represent the mean of the individual data points and the error bars are the s.e.m. ($n = 6$ independent experiments). *P*-values calculated as described in the Materials and Methods are shown.

which localizes to the PM in abundance (Jean and Kiger, 2012). Previously, Snz:GFP was shown to localize close to the PM at ER contact sites, and this localization pattern was dependent on PtdIns(4,5)P₂ (Ugrankar et al., 2019). We generated a new Snz: mCherry transgenic line, which revealed a punctate localization pattern (Fig. 4A), although it was more diffuse than that produced by Snz:GFP (see Fig. S1A). Interestingly, and consistent with the requirement of Snz for Vamp7 localization, we observed

colocalization between numerous Vamp7- and Snz-positive puncta (Fig. 4A,B). Supporting these data, we also observed the highest colocalization between SNX25-HA and GFP-VAMP8 in HeLa cells on internal puncta (as monitored through Pearson correlation; Fig. S3A,C). Importantly, SNX25 and VAMP8 co-expression in HeLa cells modified their respective localizations, resulting in increased intracellular puncta (Fig. S3A). SNX25 also showed a good degree of colocalization with the ER (indicated by calnexin)

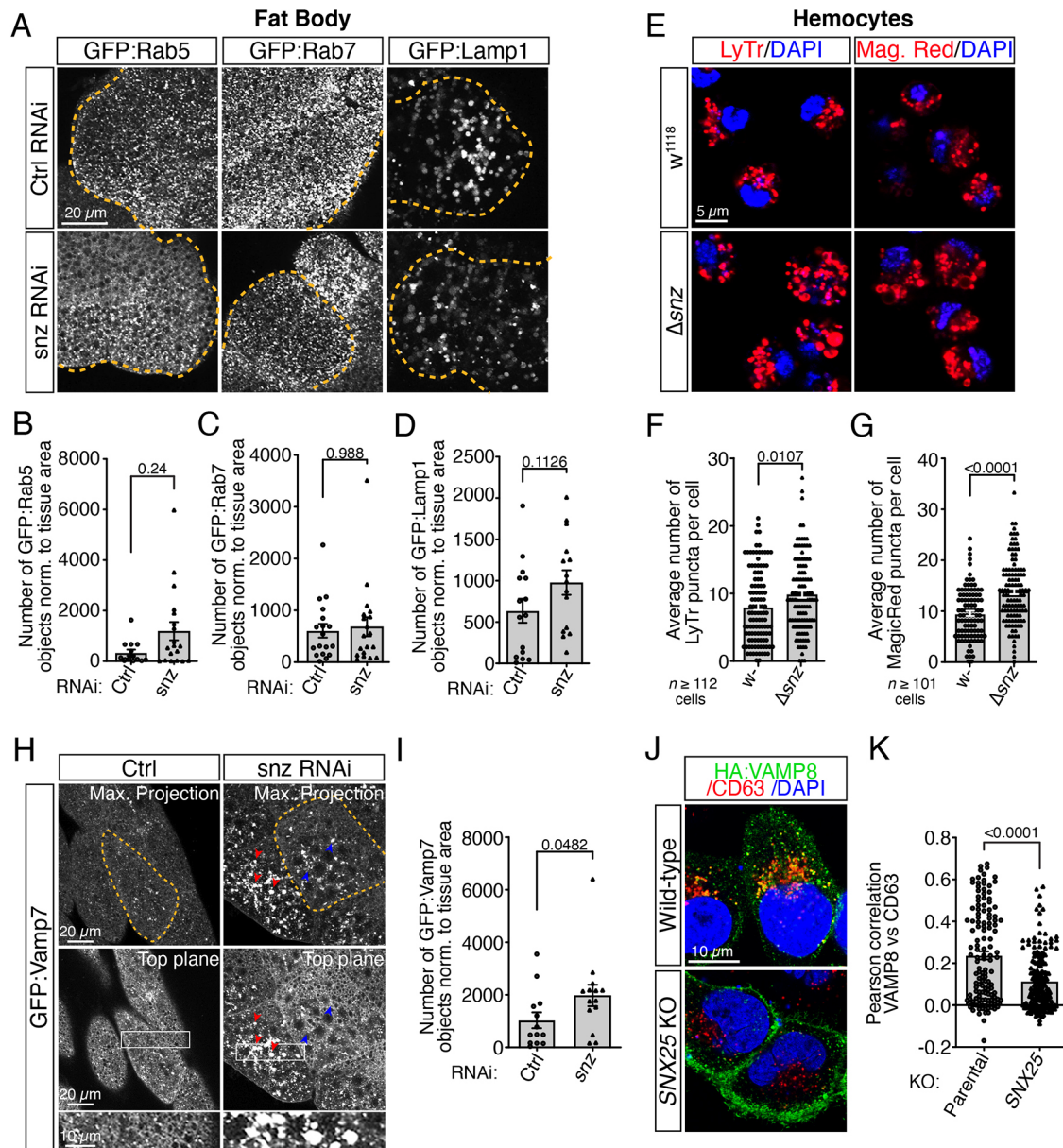


Fig. 3. Snz and SNX25 regulate Vamp7 and VAMP8 localization in fly fat body and HeLa cells, respectively. (A) Representative images of GFP:Rab5, GFP:Rab7, and GFP:Lamp1 in fed third-instar control and Snz-depleted fat bodies. Orange dotted lines indicate individual cells. (B–D) GFP:Rab5- (B), GFP:Rab7- (C), and GFP:Lamp1- (D) positive puncta were normalized to the tissue area. Bars represent the mean, individual points or triangles represent single fat body values, and the error bars are the s.e.m. ($n=4$ independent experiments for B and C, $n=3$ independent experiments for D). (E) Representative images of hemocytes bled from third instar larvae stained with either LyTr or Magic Red. (F, G) Mean LyTr (F) and Magic Red (G) puncta per cell. Bars represent the mean, individual points or triangles represent single-cell values, and the error bars are the s.e.m. ($n=3$ independent experiments). (H) Maximum projections (top panel) and single confocal sections (lower panels) of GFP:Vamp7 puncta in control and Snz-depleted cells in fed fat bodies. Blue arrowheads highlight intracellular puncta, while red arrowheads indicate aggregates present at or near the PM. The bottom panels show magnified views of the boxes in the middle panels. Orange dotted lines indicate individual cells. (I) GFP:Vamp7-positive puncta normalized to the tissue area. Bars represent the mean, individual points or triangles represent single data points, and the error bars are the s.e.m. ($n=3$ independent experiments). (J) Starved (3 h in EBSS) parental and KO HeLa cell populations transiently expressing HA-VAMP8 were fixed and stained for endogenous CD63. Nuclei were counterstained with DAPI. (K) Per-cell Pearson correlations between VAMP8 and CD63. Bars represent the mean per-cell correlation, individual points or triangles represent single data points, and the error bars are the s.e.m. ($n=3$ independent experiments). *P*-values calculated as described in the Materials and Methods are shown.

and some SNX25 puncta localized to lysosomes and LC3-positive dots, as recently observed for the SNX25 paralog SNX19 (Fig. S3A) (Saric et al., 2021). We performed a proximity ligation assay (PLA) between GFP:VAMP8 and SNX25:HA in HeLa cells, which confirmed the close proximity between GFP:VAMP8 and SNX25:HA (Fig. 4C and quantification in D). As we were unable to detect endogenous SNX25 by immunofluorescence with available

antibodies, we performed cellular fractionation experiments to examine the intracellular localization of endogenous SNX25. We observed co-fractionation of SNX25 with VAMP8 and the endosomal marker EEA1 (Fig. 4E). Interestingly, the majority of SNX25 fractionated with endosomal membranes rather than the ER, despite the fact that this protein contains two ER-anchoring hairpins (Henne et al., 2015). These results highlight the conserved

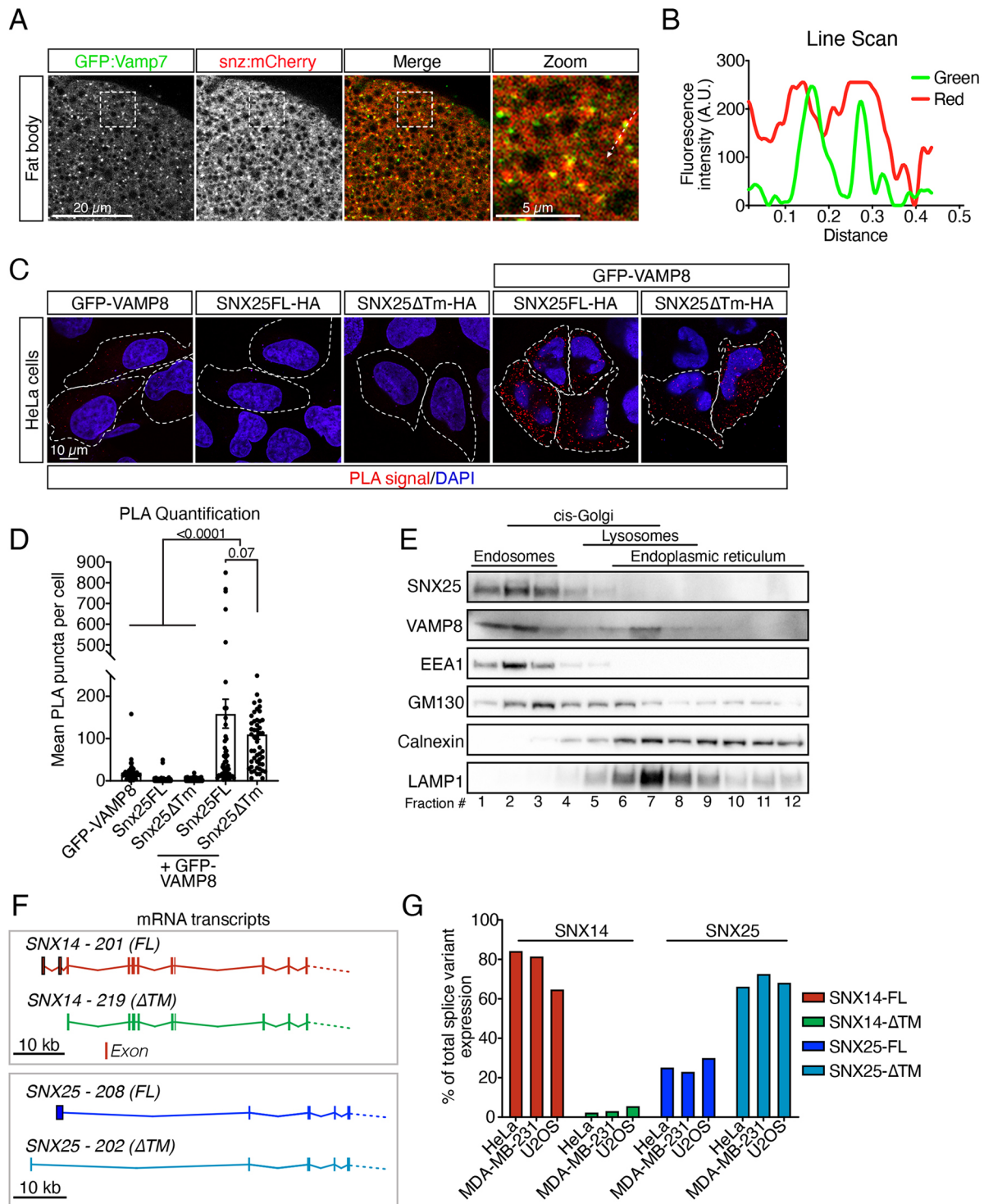


Fig. 4. Snz and SNX25 colocalize with Vamp7 and VAMP8 in flies and HeLa cells, respectively. (A) The fat bodies of fed third-instar *Drosophila* larvae co-expressing GFP:Vamp7 and Snz:mCherry were imaged by confocal microscopy. Images are representative of three independent experiments. A single z-section of the fat body surface is shown. The boxed region has been magnified. (B) Line scan of two GFP:Vamp7 puncta. The path of the line scan is indicated by an arrow in the magnified view in panel A. A.U., arbitrary units. (C) PLA immunofluorescence images showing the proximities between GFP-VAMP8 and SNX25FL-HA (full length) or SNX25ΔTM-HA (see Fig. 5A for a diagram of constructs). GFP-VAMP8, SNX25FL-HA, and SNX25ΔTM-HA were also transfected individually and probed with both antibodies as controls (first three images). PLA puncta are shown in red and nuclei were counterstained with DAPI (blue). Dotted lines define individual cells. (D) Quantification of the PLA shown in C. Bars show the mean PLA puncta per cell, individual points represent single cells, and the error bars are the s.e.m. ($n=3$ independent experiments). P -values calculated as described in the Materials and Methods are shown. (E) Immunoblot analysis of SNX25, VAMP8, EEA1, GM130, calnexin and LAMP1 after a Nycodenz gradient fractionation. Images representative of three experiments. (F) Schematic representation of the 5' transcript regions of SNX14 and SNX25. Transcript-associated numbers (from ENSEMBL) are provided, along with the presence or absence of the TM coding sequence. The TM encoding exons are highlighted by a dark border. (G) Histogram of the relative transcript levels of FL and ΔTM SNX14/SNX25 isoforms. Multiple smaller transcripts encoding different regions of SNX14 were also quantified but are not depicted in the histogram, which is why the sum of the FL and ΔTM isoforms does not equal 100%. Data representative of one experiment.

proximity between Snz/Vamp7 and SNX25/VAMP8 in flies and humans, and reveal a potential ER-independent pool of SNX25.

Different SNX14 and SNX25 isoforms are expressed in cancer cells

The fractionation result prompted us to assess whether *SNX25* (and other family members) had splice variants that could account for the observed discrepancy between the localization patterns of the endogenously and exogenously expressed proteins. In humans, *SNX14* encodes 19 transcripts, with 10 encoded proteins, while *SNX25* has eight transcripts, four of which encode proteins. Strikingly, for both *SNX14* and *SNX25*, specific coding transcripts were identified encoding isoforms lacking ER-anchoring N-terminal transmembrane (TM) domains (Fig. 4F). We thus postulated that the observed differences between the full-length (with ER anchoring) expression construct and the fractionation experiments occurred because the highest abundance SNX25 isoform in HeLa cells lacks the TM domain. Using droplet digital PCR (ddPCR), we quantified the relative abundance of full-length and TM-lacking isoforms in three independent cancer cell lines. In all three cell lines, the SNX25 isoform lacking the TM domain was more abundant than the

ER-associated isoform (Fig. 4G). In contrast, SNX14 transcripts mostly encoded longer ER-associated isoforms (Fig. 4G).

Because of the higher abundance of the truncated SNX25 isoform lacking the TM domain, we tested its localization. Unlike the ER-anchored full-length SNX25, SNX25-ΔTM was mostly cytoplasmic (Fig. S3B,C). We were not able to observe enrichment at specific sites or a clear colocalization with VAMP8; however, we did observe some proximity from the PLA (Fig. 4C,D). From these results, we conclude that in HeLa cells, SNX25 is predominantly not ER anchored and shows proximity to VAMP8.

The SNX25 PX domain is necessary for VAMP8 internalization, while ER anchoring is dispensable

The observed accumulation of VAMP8 at the PM in *SNX25* KO cells could be the result of either delayed endocytosis or impaired recycling. To test this more directly, we performed a structure–function analysis of SNX25 in HeLa cells using various truncation mutants (Fig. 5A). Using lentiviral transduction, we expressed SNX25 mutants in *SNX25* KO cells (Fig. S3D) and tracked VAMP8 internalization using an established chase assay (Jean et al., 2015; Miller et al., 2011). It is worth noting that expression of the

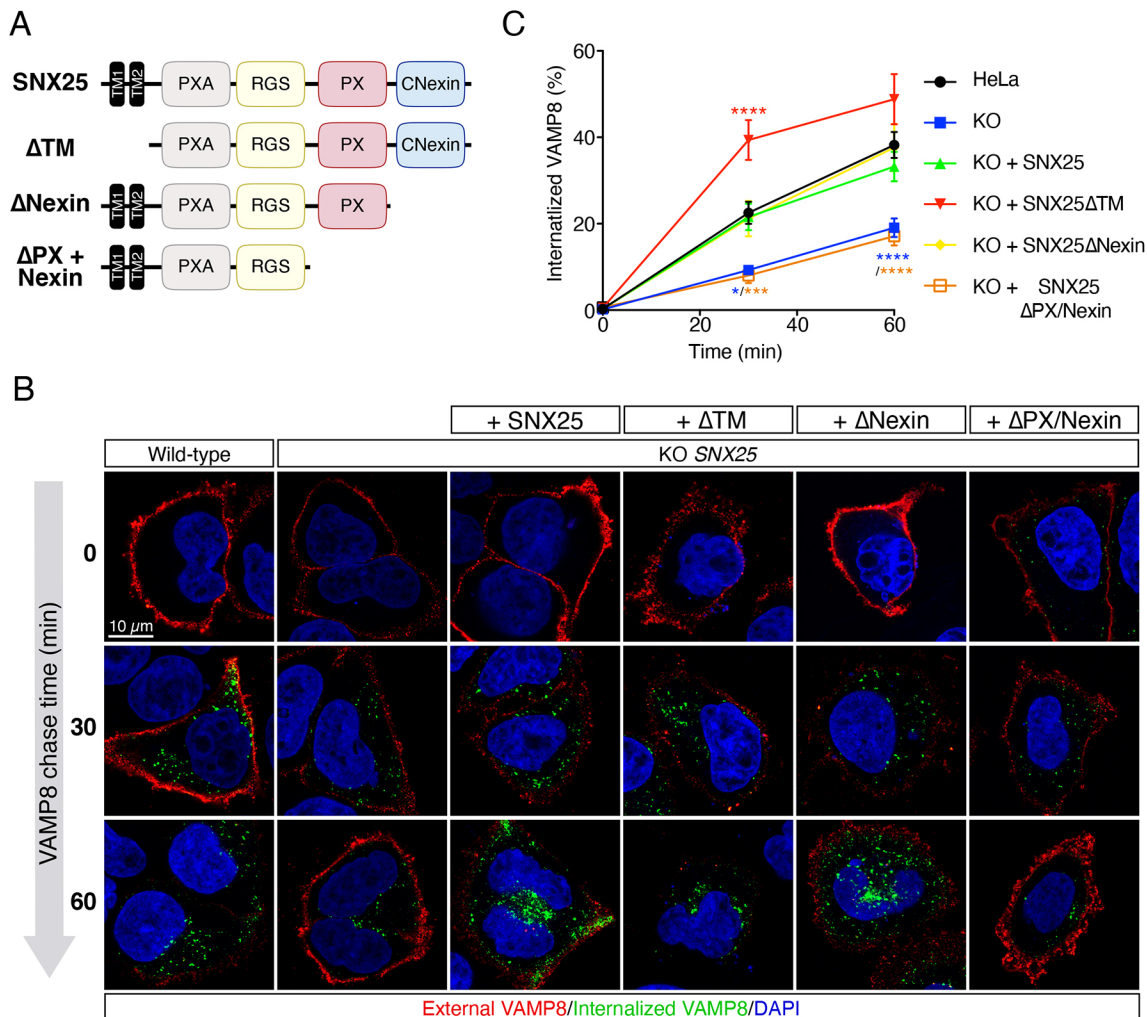


Fig. 5. The SNX25 PX domain is required for VAMP8 internalization. (A) Schematic of the SNX25 constructs used for structure/function analysis. (B) VAMP8–GFP uptake in *SNX25* KO cells expressing truncated and full-length forms of SNX25. (C) The graph shows the percentage of the total VAMP8 internalized over time, calculated by measuring the intensity of an external GFP antibody (red) and an internal GFP antibody (green). Nuclei were counterstained with DAPI. Error bars represent the s.e.m. ($n=3$ independent experiments). Statistical analyses * $P<0.05$, *** $P<0.001$ and **** $P<0.0001$ (calculated as described in the Materials and Methods).

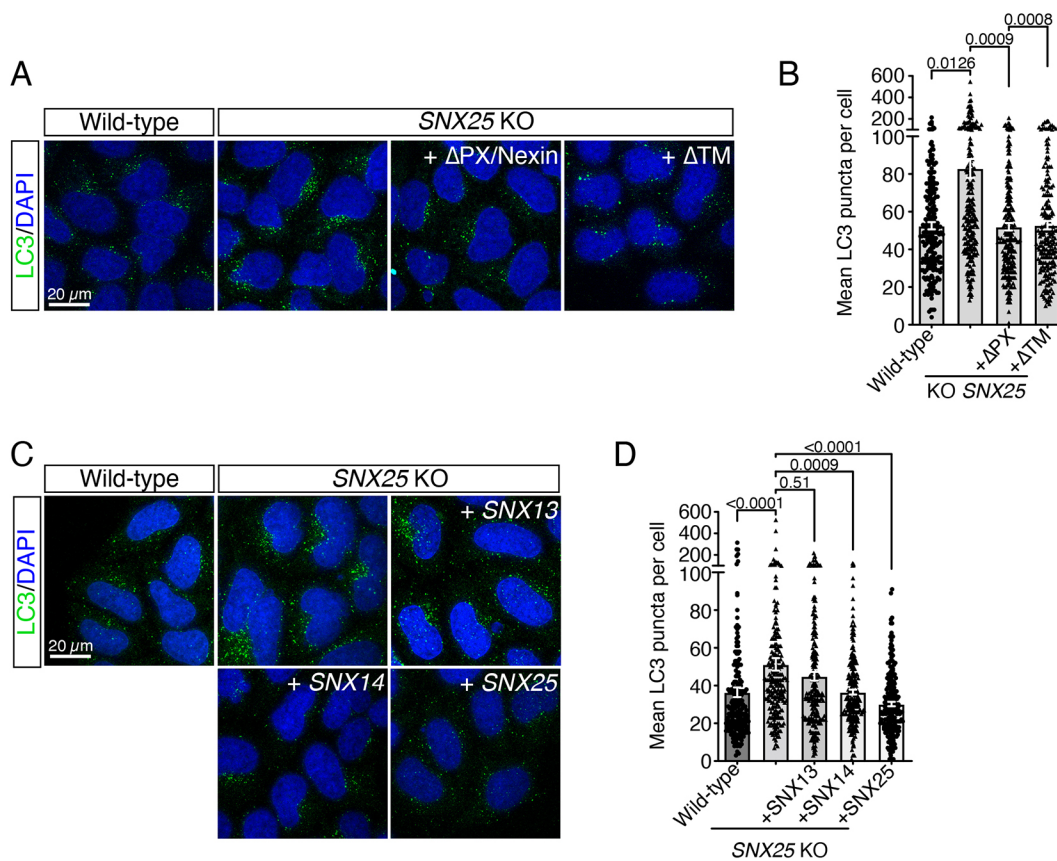


Fig. 6. SNX25 lacking its PX/Nexin or TM domains can rescue SNX25 autophagic defects. (A) Immunofluorescence analysis of endogenous LC3 (green) in wild-type or SNX25 KO HeLa cells expressing truncated forms of SNX25 grown in complete DMEM. Nuclei were counterstained with DAPI. Images are representative of three independent experiments. (B) Quantification of LC3 puncta per cell. Bars represent the mean, individual points or triangles represent single-cell values, and the error bars are the s.e.m. ($n=3$ independent experiments). (C) Immunofluorescence analysis of endogenous LC3 (green) in wild-type or SNX25 KO HeLa cells expressing full-length forms of SNX13, SNX14, or SNX25 grown in complete DMEM. Nuclei were counterstained with 4',6-diamidino-2-phenylindole (DAPI). Images are representative of three independent experiments. (D) Quantification of LC3 puncta per cell. Bars represent the mean, individual points or triangles represent single-cell values, and the error bars are the s.e.m. ($n=3$ independent experiments). P -values calculated as described in the Materials and Methods are shown.

Δ TM isoform was consistently lower compared to ER-anchored constructs, hinting at a faster turnover rate for cytoplasmic SNX25 (Fig. S3D). SNX25 KO led to decreased VAMP8 uptake (Fig. 5B,C), suggesting that increased PM VAMP8 is probably due to decreased endocytosis. This was not caused by general endocytic defects since transferrin internalization (clathrin dependent) and CD98 uptake (clathrin independent) were not affected (Fig. S4A–C). Expression of full-length SNX25 rescued VAMP8 uptake, as did the expression of SNX25 mutants missing their TM or C-terminal nexin domains (Fig. 5B,C). This indicates that ER anchoring is not required for SNX25-regulated VAMP8 uptake. However, SNX25 lacking both its PX and nexin domains could not rescue endocytosis (Fig. 5B,C). From the data, we conclude that SNX25 is required for efficient VAMP8 endocytosis, that its ER anchoring is dispensable for this regulation, and that its PX domain is required, presumably to mediate SNX25 recruitment to the PM.

Loss of SNX25 does not affect the levels or recruitment of PICALM or clathrin

Given the observed effects on VAMP8 uptake in SNX25-deficient cells, we next focused on phosphatidylinositol-binding clathrin assembly protein (PICALM), because of its essential role in small

R-SNARE internalization (Miller et al., 2011). Moreover, recent proteomic data has identified PICALM as a high confidence neighbor of SNX14-APEX2 (Datta et al., 2020). We extended this proteomic finding to SNX25, observing close proximity between SNX25 and PICALM by PLA (Fig. S4D,E). This prompted us to test for the potential misregulation of PICALM in SNX25 KO cells. Contrary to our hypothesis, no effect on PICALM localization was observed in either SNX25 KO or SNX14/SNX25 double KO cells (Fig. S4F,G), ruling out the possibility that defective VAMP8 endocytosis is caused by PICALM dysfunction. As a control in our PICALM membrane staining analysis, we monitored clathrin heavy chain localization and did not observe any reductions in recruitment (Fig. S4F,H), in agreement with the transferrin uptake data. Hence, defective VAMP8 uptake is influenced by SNX25 in a PICALM-independent manner, through a yet-to-be defined mechanism.

Defective VAMP8 endocytosis is not solely causative of the decreased autophagic flux in SNX25 KO cells

The lack of a clear endocytic phenotype in SNX25 KO cells incited us to assess whether autophagic flux could be affected by additional factors. Hence, we first monitored whether LC3 accumulation could be rescued by the Δ PX/ Δ Nexin or Δ TM mutants, which we found to

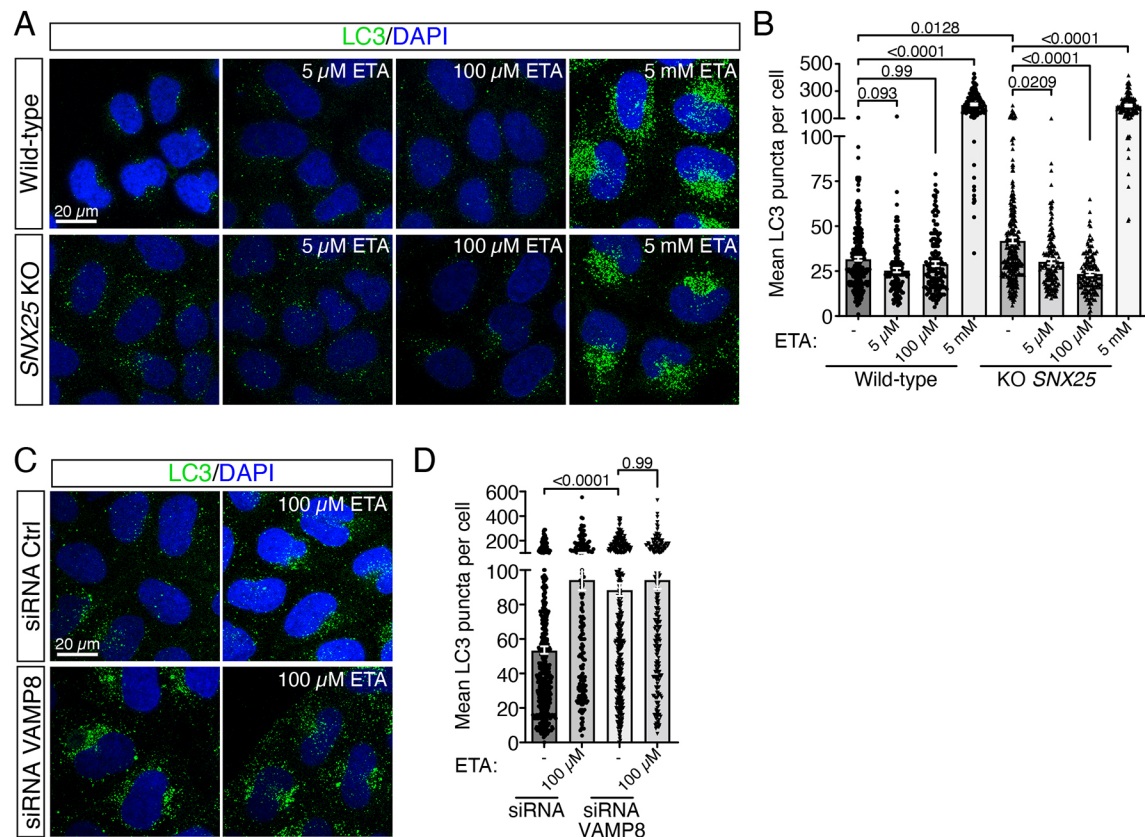


Fig. 7. SNX25 KO is rescued by ethanolamine addition, whereas VAMP8 depletion is not. (A) Immunofluorescence analysis of endogenous LC3 (green) in wild-type or SNX25 KO HeLa cells grown in complete DMEM and treated with different ETA concentration for 24 h prior to fixation. Nuclei were counterstained with DAPI. Images are representative of three independent experiments. (B) Quantification of LC3 puncta per cell. Bars represent the mean, individual points or triangles represent single-cell values, and the error bars are the s.e.m. ($n=3$ independent experiments). (C) Immunofluorescence analysis of endogenous LC3 (green) in control or VAMP8 siRNA-transfected HeLa cells grown in complete DMEM and treated with different ETA concentration 24 h prior to fixation. Nuclei were counterstained with DAPI. Images are representative of three independent experiments. (D) Quantification of LC3 puncta per cell. Bars represent the mean, individual points or triangles represent single-cell values, and the error bars are the s.e.m. ($n=3$ independent experiments). P -values calculated as described in the Materials and Methods are shown.

be ineffective and effective at rescuing VAMP8 endocytosis, respectively. SNX25 KO cells showed a higher level of LC3 puncta compared to parental HeLa cells (Fig. 6A,B), indicative of decreased autophagic flux, as observed in siRNA-treated samples (Fig. 2A–E). Interestingly, this LC3 accumulation was rescued by expression of either the Δ PX/ Δ Nexin or the Δ TM mutant (Fig. 6A,B, expression validation in Fig. S5A). These rescues are unlikely to be caused by defective autophagosome biogenesis, at least for SNX25 Δ TM, as its overexpression in wild-type cells did not affect the number of autophagosomes (Fig. S3B). This suggests that independent processes are likely affected in SNX25 KO cells. To query how specific to SNX25 these processes were, we rescued SNX25 KO HeLa cells by expressing SNX13, SNX14 or SNX25 via lentiviral transduction. Surprisingly, LC3 accumulation was rescued by both SNX14 and SNX25, but not SNX13 (Fig. 6C,D; Fig. S5B). From these structure–function analyses and the finding that SNX14 can also rescue SNX25 loss, we conclude that autophagy impairment in SNX25 KO cells results from multiple factors.

Ethanolamine addition rescues the SNX25 KO autophagic phenotype

Given the recent discovery that the PXA domain of SNX14 was important in regulating saturation levels of fatty acids, and that deletion of SNX14 also affected phosphatidylserine levels in U2OS

cells (Datta et al., 2020), we posited that a disbalance in lipid metabolism could also be involved in the phenotype. Given that ethanolamine (ETA) supplementation, which increases intracellular phosphatidylcholine levels through the Kennedy pathway, has been shown to rescue SNX4 mutants in yeast (Ma et al., 2018), we tested whether it could rescue SNX25 loss. Since a high ETA concentration was used in yeast (50 mM), while its concentration in cell culture supplements is 30 μ M, we tested the ability of 5 μ M, 100 μ M and 5 mM ETA to rescue SNX25 loss. While the low and medium concentrations did not affect the number of LC3 puncta in wild-type HeLa cells, 5 mM ETA led to a striking accumulation of LC3 puncta (Fig. 7A,B). This dramatic increase in puncta was also observed in SNX25 KO cells treated with 5 mM ETA (Fig. 7A,B). Importantly, the 5 and 100 μ M treatments revealed a dose-dependent decrease in LC3 puncta in SNX25 KO cells (Fig. 7A,B). This decrease was most likely not the result of reduced autophagosome synthesis caused by ETA addition, since a similar number of LC3 puncta were observed between wild-type and SNX25 KO cells subjected to ETA and BafA1 treatment (Fig. S5C,D). Given these results, we assessed whether VAMP8 loss could be rescued by ETA addition. As observed in yeast, ETA addition did not rescue siRNA-mediated VAMP8 loss of function (Fig. 7C,D). Altogether, these experiments suggest lipid metabolism defects in SNX25 KO cells, as that simple addition of ETA suppresses SNX25 loss but not VAMP8 depletion.

DISCUSSION

Here, we have uncovered a conserved autophagic function for *snz* and its ortholog *SNX25*. Using both RNAi-mediated depletion and CRISPR/Cas9-generated KO cells, we show that *Snz* and *SNX25* are required for full autophagic flux. We show that the impact on autophagy is unlikely to occur via lysosomal dysfunction, but potentially through a combination of inappropriate Vamp7 (in flies) and VAMP8 (in humans) internalization or trafficking and defective lipid metabolism. Interestingly, the *SNX25* PX domain was necessary for VAMP8 uptake, while ER anchoring was dispensable. Furthermore, LC3 accumulation observed upon *SNX25* loss could be rescued by *SNX25* lacking either its PX/Nexin or ER anchoring domains, and by ETA supplementation. Altogether, our findings uncover the multifaceted effects of *SNX25* loss on endocytosis and lipid metabolism, which ultimately affect autophagic flux.

To further refine the endosomal sorting regulators involved in autophagy, we performed a targeted RNAi screen of SNXs in the fly fat body and monitored autolysosome formation (Mauvezin et al., 2014; Rusten et al., 2004; Scott et al., 2004). Unexpectedly, most SNXs tested caused defects in autolysosome acidification. We believe this is a consequence of the wide range of cargos sorted or endocytosed by SNXs (Cullen, 2008). The misrouting of specific cargos could directly or indirectly affect lysosomal function and therefore autolysosome acidification or formation. Our results also reveal the potential for complementation between SNXs paralogs in mammalian cells, which may explain why autophagy defects were not observed for most SNXs in genome-wide screens (Knævelsrud et al., 2013; Moretti et al., 2018; Morita et al., 2018).

Gene redundancy and effects on autophagy

SNX14 has three paralogs in mammals – *SNX13*, *SNX19* and *SNX25*. In neural precursor cells derived from patients with SCAR20, *SNX14* loss was associated with autophagosome clearance defects (Akizu et al., 2015). Conversely, weak effects were observed in dermal fibroblasts from patients (Bryant et al., 2018). As *Drosophila* have only a single ortholog of these proteins, we were able to show through multiple approaches that loss of *Snz* affected autophagosome clearance and led to autophagosome and autophagic cargo [ref(2)P] accumulation. Our data in HeLa cells also indicate defective autophagic flux in *SNX14*- and *SNX25*-KO cells. The differences between our results and findings in patient fibroblasts might be due to differential regulation of either paralog expression or mRNA splicing between cell types. It is worth mentioning that, in HeLa cells, increased *SNX14* expression was detected upon *SNX25* KO (Fig. 2F). Furthermore, given the complementation of *SNX25* KO by *SNX14* expression, it is conceivable that *SNX25* expression could be differentially modulated in various cell types and be able to rescue *SNX14*-linked autophagic defects.

Our data indicate defects in the trafficking of Vamp7 and VAMP8 after depletion of *Snz* and *SNX25*, respectively (Fig. 3H and J). Since the YKT6–SNAP29–STX7 complex can also promote autophagosome–lysosome fusion, it is likely that this complex partially complements the loss of *Snz* and *SNX25*, which would explain why their loss did not completely abrogate autophagic flux. Along these lines, differential expression of SNARE complexes between cell types could also account for the variations in penetrance observed between *SNX14* studies (Knævelsrud et al., 2013; Moretti et al., 2018; Morita et al., 2018).

Roles for *SNX25* in endocytosis and its link to autophagy

How exactly *Snz*/*SNX25* regulates Vamp7/VAMP8 endocytosis or trafficking remains to be defined. We were unable to directly test

Vamp7 trafficking in flies; however, we did observe ectopic accumulation of GFP:Vamp7 puncta near or at the PM, suggesting a potential uptake defect (Fig. 3H). To test this more directly, we assessed VAMP8 uptake in *SNX25* KO cells. Interestingly, these cells showed decreased VAMP8 internalization that was dependent on the *SNX25* PX domain, which interacts with diphosphorylated phosphoinositides (Chandra et al., 2019; Mas et al., 2014) like PtdIns(4,5)P₂, which is highly abundant at the PM (Jean and Kiger, 2012). We did not observe defects in clathrin-dependent or -independent endocytosis, nor variations in clathrin recruitment at the PM. Hence, it is unlikely that *SNX25* depletion results in VAMP8 trafficking defects by affecting PtdIns(4,5)P₂ or PtdIns(3,4)P₂ dynamics at the PM. Recently, *Snz* was demonstrated to bridge PM–ER contact sites to modulate LD formation (Ugrankar et al., 2019). Therefore, *SNX25* may fulfill a similar function in mammals, bridging PM–ER contact sites to favor VAMP8 internalization. A precedent for the involvement of ER–PM contact sites in endocytosis exists (Conte et al., 2017); however, we could rescue VAMP8 internalization in *SNX25* KO cells with a transgene lacking its ER-anchoring domains, implying that ER–PM proximity is not required for efficient VAMP8 uptake. This notion is consistent with the known requirement of PICALM for VAMP8 uptake (Miller et al., 2011; Moreau et al., 2014). Surprisingly, we did not detect any defects in PICALM localization in *SNX25* or *SNX14*/*SNX25* KO cells, although we did observe close proximity between it and overexpressed *SNX25*. VAMP8 can also be internalized through a clathrin-independent pathway stimulated by Shiga toxin (Renard et al., 2015). This pathway is dependent on lipid organization and might be perturbed in *SNX25* KO cells. An earlier study identified *SNX25* as a regulator of transforming growth factor β receptor (TGF β R) endocytosis. However, this study erroneously characterized the Δ TM isoform of *SNX25* and showed that overexpression of this short isoform increased TGF β R internalization (Hao et al., 2011), while *SNX25* knockdown decreased uptake. Thus, *Snz*/*SNX25* might affect the endocytosis of multiple cargos, in addition to Vamp7 and VAMP8.

It is also worth mentioning that the yeast ortholog of *snz* and *SNX25*, *MDM1*, was originally identified as a regulator of endocytic trafficking (Henne et al., 2015), thus other aspects of trafficking could be impaired in *Snz*/*SNX25* mutants and be sensitive to protein expression levels. Although our data illustrate decreased internalization of VAMP8 in *SNX25* KO cells, the possibility remains that VAMP8, in addition to its uptake defect, could be misrouted on route to autolysosomes. We did observe decreased colocalization between VAMP8 and CD63 in *SNX25* KO cells; therefore, defective trafficking cannot be ruled out. Moreover, co-expression of both *SNX25* and VAMP8 led to the re-localization of both proteins to large internal vesicles. This effect required the TM region of *SNX25*, thus it is conceivable that although the short isoform is sufficient for VAMP8 internalization, the longer ER-associated isoform could regulate the endosomal sorting of VAMP8, through potential inter-organellar contact sites or by modulating lipid metabolism (Datta et al., 2020).

SNX25 and its ortholog in lipid metabolism and link to autophagy

Recent studies have demonstrated important roles for *SNX14* in lipid metabolism (Bryant et al., 2018; Datta et al., 2019, 2020; Hariri et al., 2019). *SNX14* loss results in saturated fatty acid accumulation and increased sensitivity to lipotoxic stress. Moreover, *SNX14*, *Snz* and *Mdm1*, the yeast ortholog, all regulate LD formation (Bryant et al., 2018; Datta et al., 2019; Hariri et al., 2018, 2019;

Ugrankar et al., 2019). The functional domains required for SNX14 regulation of LD formation differ from the ones required in SNX25 for VAMP8 uptake; the TM and C-terminal nexin domains of SNX14 are essential for LD localization and regulation (Datta et al., 2019), while the PX domain of SNX25 is required for VAMP8 uptake, and its TM domains are dispensable. Interestingly, LD biogenesis, fatty acid trafficking and autophagy are known to intersect (Nguyen et al., 2017; Rambold et al., 2015). In this context, it is tempting to speculate that Snz and its human orthologs SNX14 and SNX25 could bridge lipid stress and autophagy regulation. Further supporting this hypothesis is the finding that SNX25 loss can be rescued by SNX14 or by either SNX25 Δ TM and SNX25 Δ PX/Nexin. Moreover, ETA addition, which is predicted to result in higher intracellular phosphatidylethanolamine levels (Ma et al., 2018; Patel and Witt, 2017), rescued SNX25 deletion. These rescue experiments highlight that SNX25 loss causes independent phenotypes that culminate in decreased autophagic flux. The effects are likely more potent in flies, since they have a single ortholog and our data show that SNX14 can efficiently rescue SNX25 loss. Concerning the role of SNX25 in lipid metabolism, it is tempting to speculate that it is most probably linked to an effect on lipid saturation and LD biogenesis for four main reasons. First, the C-Nexin region of SNX14 was shown to mediate LD localization, and we could rescue SNX25 loss using a SNX25 mutant deleted of this region, arguing that LD recruitment of SNX25 is dispensable. Second, our KO/rescue experiments in HeLa cells were performed in normal growth conditions, where LD biogenesis is minimal, and thus unlikely to affect autophagy. Third, recent findings in U2OS cells identified the PXA region of SNX14 as important in regulating lipid saturation and ER stress in response to saturated lipid accumulation (Datta et al., 2020). As the PXA was conserved in the two rescue constructs used for autophagy rescue, it is plausible that SNX25 somehow affects lipid homeostasis and thus autophagosome–lysosome fusion. Moreover, recent findings illustrated the importance of the PE ratio in membrane fusion (Ma et al., 2018; Tornø and Wickner, 2021), and SNX14 deletion leads to increased phosphatidylserine levels (Datta et al., 2020) as in SNX4 yeast mutants (Ma et al., 2018). This intriguing possibility warrants further studies to identify the specific determinants that mediate the action of SNX25 in endocytosis versus lipid homeostasis.

Another possibility to consider is that SNX25 may encode a lipid clustering or transport domain that could help concentrate lipids or move them between organelles in a manner that support functional autophagy. In support of this, recent work using AlphaFold2 structural predictions suggest that the Nexin-C and PXA domains of the yeast SNX25 ortholog Mdm1 fold together to create a large spherical domain with a hydrophobic channel that could, in principle, ferry lipids between organelles at organelle contacts (Castro et al., 2021 preprint). Such a domain could enable SNX25 to localize to various intracellular sites, and cluster and/or transport lipids to support functional autophagy. SNX14 is predicted to contain this domain arrangement as well and this might explain why it can rescue SNX25 loss. In this model, loss of SNX25 would alter lipid homeostasis and subcellular distribution, leading to defects in Vamp7/VAMP8 trafficking and functional autophagy. The molecular details for this process, however, remain to be addressed.

Potential impacts of differentially spliced SNX14 and SNX25

The observation that various isoforms of SNX14 and SNX25 are expressed in cells is intriguing. This raises the possibility of functional pools of SNX14 and SNX25, with the longer ER-anchored isoform regulating LD biogenesis and the shorter isoforms regulating other processes, like trafficking and autophagy. It is

worth noting, however, that although we provide evidence from ddPCR experiments, we were unable to demonstrate differential splicing at the protein level because of a lack of isoform-specific antibodies. Isoform expression may be controlled by modulating splicing in response to stress, as has been observed for multiple genes (Biamonti and Cáceres, 2009). Alternatively, different transcription factors may favor the expression of certain isoforms (Babeu et al., 2018). RNA-sequencing datasets from *Drosophila* do not contain different Snz isoforms, suggesting that a single isoform regulates both LD biogenesis and autophagy.

Conclusions

In summary, we have identified a new role for *snz* and its ortholog SNX25 in autophagy regulation through effects on Vamp7/VAMP8 internalization and lipid metabolism. Moreover, we described differentially expressed isoforms of SNX14 and SNX25 in cancer cells. Based on our results and those of previous studies (Akizu et al., 2015; Bryant et al., 2018), we propose that Snz and SNX25 finetune the endocytosis/trafficking of Vamp7 and VAMP8 and potentially regulate the lipid composition of endolysosomes to coordinate the autophagy level with the demands of the cell. It will be interesting to define how these functions differ between various genes and isoforms, and how they are affected by different stressors.

MATERIALS AND METHODS

Drosophila strains

Cg-Gal4 was used to drive UAS-RNAi hairpin expression in the fat body and hemocytes. Genotypes used in this study include: (1) *w; UAS-IR-Snz^{V105671}*, (2) *Δ snazarus* (from Ugrankar et al., 2019), (3) *w; UASp-GFP:mCherry:Atg8a* (from Ioannis Nezis, University of Warwick, Warwick, UK), (4) *y¹ sc^v v¹ sev²¹; P{TriP.GL01875}attP40* (Bloomington 67953); SNX1 RNAi, (5) *w; UAS-IR-SNX3^{V104494}*, (6) *w; UAS-IR-SNX6^{V24275}*, (7) *w; UAS-IR-SNX17^{V109452}*, (8) *w; UAS-IR-SNX18^{V22412}*, (9) *w; UAS-IR-SNX21^{V101320}*, (10) *w; UAS-IR-SNX23^{V40603}*, (11) *w; UAS-IR-SNX27^{V108542}*, (12) *w; UAS-Snz:GFP* (from Ugrankar et al., 2019), (13) *w; Cg-GAL4, UAS-GFP:Vamp7³/CyO* (from Jean et al., 2015), (14) *w; Cg-GAL4, UAS-GFP:Lamp1* (from Jean et al., 2015), (15) *w; Cg-GAL4, UAS-GFP:Rab7²* (from Jean et al., 2015), and (16) *w; Cg-GAL4, UAS-GFP:Rab5* (from Jean et al., 2015).

New lines generated in this study were: (1) *w; Cg-Gal4; p{w[mC]=UAS-Snz:GFP}*, (2) *w; p{w[mC]=UAS-Snz:mCherry}*.

Drosophila crosses and starvation protocol

Fly stocks were maintained on standard cornmeal food (Bloomington). Fly crosses were housed at room temperature for 2 days, then shifted to 29°C for 3 days. To ensure that third-instar larvae were not crowded, 20–30 larvae were transferred to new vials 16–20 h before experiments. Actively feeding third-instar larvae were starved by incubating them on Kimwipes prewetted with 1× phosphate-buffered saline (PBS) for 3 h at 25°C.

Immunofluorescence, uptake assays, PLA and microscopy

Fed or starved fat bodies were imaged live and dissected in 1× PBS. For LyTr experiments, fat bodies were incubated in a 1:5000 dilution in 1× PBS of LyTr (Thermo Fisher Scientific) for 5 min at room temperature and washed once in 1× PBS. For all other conditions, fat bodies were dissected in 1× PBS only. Fat bodies were mounted on #1.5 coverslips using silicone grease and five individual fat bodies per condition were imaged per experiment. For ref(2)P experiments, fed third-instar larvae were inverted and fixed for at least 2 h in 1× PBS containing 8% paraformaldehyde. Larvae were blocked and permeabilized by a 2 h incubation at room temperature in 1× PBS containing 5% goat serum, 1% bovine serum albumin (BSA) and 0.3% Triton X-100. Larvae were incubated overnight at 4°C in 1:500 anti-ref(2)P antibody (Abcam, ab178440) diluted in 1× PBS containing 1% BSA and 0.3% Triton X-100. Larvae were washed five times for 5 min each in 1× PBS at room temperature and incubated with secondary

antibodies (1:250, anti-rabbit-IgG conjugated to Alexa Fluor 488; Life Technologies) for 2 h at room temperature. Larvae were washed as above, and fat bodies were dissected and mounted in 1× PBS for imaging.

Wild type, siRNA-treated, and KO HeLa cells were seeded on #1.5 coverslips and treated according to the various experimental schemes. All immunofluorescence experiments were performed on HeLa cells grown in complete (full) Dulbecco's modified Eagle's medium [DMEM; supplemented with 10% fetal bovine serum (Wisent, Saint-Bruno, QC, Canada) and 1% penicillin/streptomycin], unless otherwise mentioned. HeLa were starved in Earle's balanced salt solution (EBSS) for 3 h. Ethanolamine was added to complete DMEM at a final concentration of 5 μ M, 100 μ M, or 5 mM for 24 h. Cells were fixed in 4% paraformaldehyde and immunofluorescence was performed following the Cell Signaling Technology protocol. Magic Red (ImmunoChemistry Technologies, Bloomington, MN, USA) staining was performed following the manufacturer's instructions, and live cells were analyzed on a Celldiscoverer 7 (Zeiss) equipped with an environmental chamber. Antibodies used for immunofluorescence were: anti-GFP (1:500, MilliporeSigma, 11814460001), anti-HA (1:1000, Cell Signaling Technology, Danvers, MA, USA, 3724), anti-CD63 (1:250, BD Biosciences, 561983), anti-LC3 (1:1600, Cell Signaling Technology, 12741), anti-APPL1 (1:200, Cell Signaling Technology, 3858), anti-EEA1 (1:100, Cell Signaling Technology, 3288), anti-calnexin (1:50, Cell Signaling Technology, 2679), anti-GM130 (1:3000, Cell Signaling Technology, 12480), anti-PICALM (1:200, Abcam ab172962), and anti-clathrin heavy chain (1:50, Cell Signaling Technology, 4796). Secondary antibodies [anti-mouse-IgG conjugated to Alexa Fluor 546 (#A11003), anti-rabbit-IgG conjugated to Alexa Fluor 546 (#A11035), anti-mouse-IgG conjugated to Alexa Fluor 488 (#A11029), and anti-rabbit-IgG conjugated to Alexa Fluor 488 (#A11008)] were purchased from Thermo Fisher Scientific (Waltham, MA, USA) and used at 1:500. Cells were counterstained with DAPI (1:10,000, Cell Signaling Technology).

PLA experiments were performed as previously described (Del Olmo et al., 2019b), except that the primary antibodies used for the PLA reaction were anti-HA (1:1000, Santa Cruz Biotechnology, Dallas, TX, USA, 7392) and anti-GFP (1:500, Thermo Fisher Scientific, A6455). Transferrin and CD98 uptake assays were performed as previously described (Del Olmo et al., 2019a). Finally, VAMP8 uptake assays were performed as described (Jean and Kiger, 2016) except that VAMP8-GFP was used instead of VAMP8-3×HA. A 1:100 dilution of anti-GFP (MilliporeSigma, 11814460001) was diluted in complete DMEM and used to chase VAMP8-GFP uptake. Secondary antibodies used for uptake experiments were anti-mouse-IgG conjugated to Alexa Fluor 555 (#A32727) and anti-mouse-IgG conjugated to Alexa Fluor 647 (#A32728) from Thermo Fisher Scientific.

Images were acquired on an Olympus FV1000 microscope with a UPlanSApo 40×1.3 NA oil objective (in Fig. 1A,C,G, Fig. 3A,H, Figs S1B and S3A), a Zeiss LSM 880 microscope with a W PlanAPO 40×1.4 NA oil objective (Figs 2D, 3E,J, 4A–C, 5B, 6, 7, Figs S1A,C,F, S2E, S3A,B, S4A,D–F, and S5A–C), or a Celldiscoverer 7 using a Plan-Apochromat 20× WD 0.8 NA objective (Fig. S2A). Samples with the strongest signals (e.g. a starved fat body for LyTr) were imaged first to set acquisition parameters, which were conserved for all samples in the same experimental set to avoid the saturation of strong samples and ensure that the full intensity scale was used for each experiment. Images were exported to .tiff files without compression using ZEN Blue (Zeiss) and quantified using Cell Profiler as previously described (Jean et al., 2015). Similar thresholding and object identification were used throughout image analysis. Criteria were set to allow the identification of strong and medium intensity puncta only, excluding puncta with intensities close to background levels. Images were prepared for publication using Photoshop 2021 (Adobe, San Jose, CA, USA). Only linear level adjustments were performed, which were kept consistent between experimental sets and for data representation. Enhanced images were cropped and merged in Photoshop and assembled in Adobe Illustrator.

Generation of DNA constructs

Full-length *Snz*:GFP was used to generate the *Snz*:mCherry construct. Briefly, the *snz* coding region (from *Snz*:GFP) and mCherry (from

pmCherry-C1) were PCR amplified and ligated into the pUAST-Attb plasmid using the In-FusionHD Cloning Kit (Takara Bio, Mountain View, CA, USA). The plasmid was injected into flies by Genome Prolab. Full-length *SNX25* was PCR amplified from HeLa cell cDNA generated with the Superscript III First-Strand Synthesis System (Thermo Fisher Scientific) and cloned into pcDNA3-3×HA using the In-FusionHD Cloning Kit. This plasmid was used as a template to generate the various truncation mutants. Lentiviral vectors were generated by subcloning the different pcDNA3-SNX25-HA mutants into a BamHI/AfeI-digested pLVX vector using the In-FusionHD Cloning Kit. All vectors generated were validated by sequencing.

Cell culture, CRISPR/Cas9 KO and lentiviral rescue

HeLa cells, a kind gift of Dr Tamotsu Yoshimori (Osaka University, Osaka, Japan), were maintained in complete DMEM at 37°C and 5% CO₂ and frequently tested for mycoplasma contamination. Transient plasmid and siRNA transfections were performed with JetPrime (PolyPlus-transfection, New York, NY, USA) and Dharmafect (Dharmacon, Lafayette, CO, USA), respectively, according to the manufacturers' instructions. Cells were analyzed by western blotting or immunofluorescence 24 h after plasmid transfection and 72 h after siRNA transfection. The siRNAs from Dharmacon used were: SNX13-1 (J-009381-10-0002), SNX13-2 (J-009381-11-0002), SNX14-1 (J-013190-10-0002), SNX14-2 (J-013190-12-0002), SNX25-1 (J-014761-11-0002), SNX25-2 (J-014761-12-0002), SNX19-1 (J-029832-10-0002), SNX19-2 (J-029832-11-0002), VAMP8 (J-013503-05-0002) and a non-targeting control (scramble, D-001810-01-05), at a final concentration of 10 nM. Knockdown efficiencies were measured by quantitative reverse transcription (qRT)-PCR, and relative mRNA levels were calculated using the $\Delta\Delta$ CT method (Livak and Schmittgen, 2001) and normalized to levels of glyceraldehyde 3-phosphate dehydrogenase (*GAPDH*) (Del Olmo et al., 2019b).

KO HeLa cell populations were generated as previously described (Del Olmo et al., 2019a). Briefly, three independent gRNAs per gene (sequences obtained from Sullender et al., 2016) were cloned into pX330A and validated by sequencing. Cells were transfected with the three gRNAs along with the pEGFP-Puro plasmid using JetPrime at a 10:1 ratio (300 ng of each pX330A-gRNA and 100 ng of pEGFP-Puro). The following day, transfected cells were selected for 36 h with puromycin (1 μ g/ml), followed by expansion in complete DMEM for two passages. KO efficiencies were then validated by western blot analysis. KO cell populations were used at low passage numbers for all experiments, to ensure that residual wild-type cells would not outcompete edited cells. Multiple independent populations for each gene were generated and used throughout the study.

For KO/rescue experiments, lentiviruses were produced in 293T cells and supernatants were collected and stored. *SNX25* KO cells were transduced with the various lentiviruses and selected with puromycin (1 μ g/ml) for 2 days. Following selection, cells were expanded for one passage and used in experiments. Expression of the various rescue constructs was confirmed by western blot analysis (Fig. S3D) or fluorescence (Fig. S5A,B).

Western blot analysis

To analyze autophagy, HeLa cells (5×10^4 cells for siRNA transfections or 2×10^5 KO cells) were seeded in individual wells of a 24-well plate. Cells transfected with siRNA were processed 72 h after transfection, while KO cells were processed 24 h after plating. Cells were lysed in 150 μ l radioimmunoprecipitation (RIPA) buffer [20 mM Tris-HCl pH 7.5, 150 mM NaCl, 1 mM ethylenediaminetetraacetic acid (EDTA), 1 mM ethylene glycol tetraacetic acid, 1% NP-40, 0.1% sodium dodecyl sulfate (SDS), and 2× protease inhibitors (Sigma-Aldrich, St Louis, MO, USA)] for 20 min on ice. Protein extracts were centrifuged at 15,900 *g* for 10 min at 4°C. Supernatants were collected and quantified using the Pierce BCA Protein Assay Kit (Thermo Fisher Scientific). Equal amounts of proteins were resolved by SDS-PAGE and transferred to PVDF (Immobilon) membranes. The following antibodies were used for western blot analysis: anti-LC3 (1:1000, Cell Signaling Technology, 12741), anti-SNX14 (1:500, Sigma-Aldrich, hpa017639), anti-SNX25 (1:500, Abcam, ab183756), anti-tubulin (1:2500, Sigma-Aldrich, T9026), anti-VAMP8 (1:1000, Synaptic Systems, Göttingen, Germany, 104302), anti-EEA1 (1:1000, Cell Signaling Technology, 3288), anti-GM130 (1:1000, Cell Signaling Technology,

12480), anti-calnexin (1:1000, Cell Signaling Technology, 2679), anti-LAMP1 (1:1000, Cell Signaling Technology, 9091), anti-ref(2)P (1:500, Abcam, ab178440), anti-GAPDH (1:2000, Cell Signaling Technology, 8884), anti-EGFR (1:1000, Cell Signaling Technology, 4267), anti-phosphorylated-ERK Thr 202/204 (1:1000, Cell Signaling Technology, 4370) and anti-HA (1:1000, Cell Signaling Technology, 3724). Horseradish peroxidase-coupled secondary antibodies were purchased from Jackson ImmunoResearch (West Grove, PA, USA). Bands were detected by chemiluminescence using Luminata Forte (Millipore).

Analysis of ref(2)P (a kind gift from Gabor Juhasz, Eötvös Lorand University, Budapest, Hungary) in fat bodies was performed as described (Jean et al., 2015) with a few modifications. Briefly, five third instar control or Snz RNAi-expressing larvae were dissected, and all fat body tissues removed. Fat bodies were lysed directly in 100 µl of 1× Laemmli buffer for 20 min at 4°C. Fat body extracts were centrifuged at 15,900 *g* for 10 min at 4°C. Each supernatant was collected and 25 µl was loaded directly on an 8% SDS-PAGE gel and analyzed by western blotting as described above.

Protein fractionation

Cell fractionation was performed as previously described (Reekmans et al., 2010) with some modifications. Briefly, for each sample, two confluent 150 mm plates of HeLa cells were washed twice with ice-cold 1× PBS, trypsinized, and resuspended in DMEM. Cells were centrifuged at 500 *g* for 5 min and washed twice in ice-cold 1× PBS. Each cell pellet was resuspended in 10 mM triethanolamine (pH 7.4), 10 mM acetic acid, 250 mM sucrose, 1 mM EDTA, 1 mM dithiothreitol and 1× protease inhibitor. Cells were homogenized using a Dounce homogenizer and centrifuged at 500 *g* for 10 min at 4°C. The supernatant was collected and loaded on a 10–25% Nycodenz (Sigma-Aldrich) continuous gradient. The gradient was centrifuged for 90 min at 170,000 *g* in a swinging bucket rotor. Twelve 1-ml fractions were collected from the top to the bottom of the gradient using a P1000 manual pipettor. Fractions were precipitated using trichloroacetic acid and resuspended in 100 µl of 1× Laemmli buffer, and 25 µl was resolved by SDS-PAGE and analyzed as described above.

EGFR degradation

HeLa cell KO populations were cultured to 80% confluence, serum starved for 16 h, and treated with 100 ng/ml EGF and 25 µg/ml cycloheximide for the indicated period of time (Jean et al., 2015). Cells were then lysed in RIPA buffer, processed and analyzed as described above.

ddPCR

Primers were designed as described elsewhere (Brosseau et al., 2010). All primers were individually resuspended to 20–100 µM in Tris-EDTA buffer (IDT) and diluted as primer pairs to 1 µM in RNase DNase-free water (IDT). Primer validation was performed on a CFX96 Real-Time PCR Detection System (Bio-Rad) with 5 µl of 2× PerfeCTa SYBR Green SuperMix Reagent (QuantaBio, Beverly, MA, USA). Amplified products were analyzed by automated chip-based microcapillary electrophoresis on a Labchip GX Touch HT Nucleic Acid Analyzer (Perkin Elmer). Primer sequences are listed in Table S1.

For ddPCR, reactions were composed of 10 µl of 2× QX200 ddPCR EvaGreen Supermix (Bio-Rad), 3 µl (150 ng) cDNA, 4 µl paired primers (final concentration: 200 nM), and 3 µl molecular grade sterile water (Wisent) in a 20 µl total reaction. Reactions were converted to droplets with the QX200 Droplet Generator (Bio-Rad). Droplet-partitioned samples were then transferred to a 96-well plate. The plate was sealed, and ddPCR was performed in a C1000 Touch Thermal Cycler (Bio-Rad). The plate was then transferred to a QX200 Droplet Reader and read (Bio-Rad). The concentrations (in copies/µl) of the final 1× ddPCR reactions were determined using QuantaSoft software (Bio-Rad) and the abundance of each transcript was normalized to the total transcript abundance.

Experimental design and statistical analysis

The RNAi screen presented in Fig. 1A was performed in independent duplicates for each RNAi. Five genes were screened along with a starved control. Independent data sets were pooled and graphed as in Fig. 1B. All

other experiments performed in the fly fat body were performed in at least three independent replicates, as were all experiments performed in HeLa cells.

Statistical analyses were performed using GraphPad Prism (GraphPad Software, San Diego, CA, USA) and all graphs show individual data points and the standard error of the mean (s.e.m.) to ease the analysis of experimental variations. For some quantifications (where curves are depicted) only the s.e.m. are displayed. For statistical analyses, normality was first assessed using a D'Agostino-Pearson omnibus normality test. Samples with normal distributions were analyzed by unpaired two-tailed *t*-tests, while nonparametric Mann-Whitney tests were performed for samples with non-normal distributions. Multiple samples were compared using two-way analysis of variance (Fig. 5C).

Acknowledgements

We thank members of the Jean laboratory for their helpful opinions during this work and Amy Kiger for her support in establishing tools for this study. We thank Alexander Sorkin for generously providing the GFP-PICALM plasmid. We thank the Photonic microscopy platform for confocal use, and the RNomics platform for primer design and for performing ddPCR reactions. We thank High-Fidelity Science Communications for editing the manuscript. Steve Jean is a member of the Fonds de Recherche du Québec - Santé (FRQS)-Funded Centre de Recherche du CHUS and is a recipient of a Research Chair from the Centre de recherche médicale de l'Université de Sherbrooke.

Competing interests

The authors declare no competing or financial interests.

Author contributions

Conceptualization: S.J.; Methodology: A.L., M.B., R.L., S.N., S.J.; Formal analysis: A.L., S.J.; Resources: R.U., M.H.; Data curation: A.L., M.B.; Writing - original draft: S.J.; Writing - review & editing: S.J.; Visualization: A.L., M.B., S.J.; Supervision: S.J.; Funding acquisition: S.J.

Funding

This research was supported by an operating grant from the Canadian Institutes of Health Research (CIHR; MOP 142305). Marie-France Bossanyi was supported by master's degree fellowships from the Natural Sciences and Engineering Research Council of Canada and Fonds de Recherche du Québec - Santé (FRQS) and Sonya Nassari by a postdoctoral fellowship from the FRQS. Steve Jean is supported by junior faculty salary awards from CIHR and FQRS (FRQS-J1 and J2).

Peer review history

The peer review history is available online at <https://journals.biologists.com/jcs/article-lookup/doi/10.1242/jcs.258733>.

References

- Akizu, N., Cantagrel, V., Zaki, M. S., Al-Gazali, L., Wang, X., Rosti, R. O., Dikoglu, E., Gelot, A. B., Rosti, B., Vaux, K. K. et al. (2015). Biallelic mutations in SNX14 cause a syndromic form of cerebellar atrophy and lysosome-autophagosome dysfunction. *Nat. Genet.* **47**, 528–534. doi:10.1038/ng.3256
- Antón, Z., Betin, V. M. S., Simonetti, B., Traer, C. J., Attar, N., Cullen, P. J. and Lane, J. D. (2020). A heterodimeric SNX4-SNX7 SNX-BAR autophagy complex coordinates ATG9A trafficking for efficient autophagosome assembly. *J. Cell Sci.* **133**, jcs246306. doi:10.1242/jcs.246306
- Baba, T., Toth, D. J., Sengupta, N., Kim, Y. J. and Balla, T. (2019). Phosphatidylinositol 4,5-bisphosphate controls Rab7 and PLEKMH1 membrane cycling during autophagosome-lysosome fusion. *EMBO J.* **38**, e100312. doi:10.15252/embj.2019102837
- Babeu, J.-P., Jones, C., Geha, S., Carrier, J. C. and Boudreau, F. (2018). P1 promoter-driven HNF4α isoforms are specifically repressed by β-catenin signaling in colorectal cancer cells. *J. Cell Sci.* **131**, jcs214734. doi:10.1242/jcs.214734
- Bas, L., Papinski, D., Licheva, M., Torggler, R., Rohringer, S., Schuschnig, M. and Kraft, C. (2018). Reconstitution reveals Ykt6 as the autophagosomal SNARE in autophagosome-vacuole fusion. *J. Cell Biol.* **217**, 3656–3669. doi:10.1083/jcb.201804028
- Biamonti, G. and Caceres, J. F. (2009). Cellular stress and RNA splicing. *Trends Biochem. Sci.* **34**, 146–153. doi:10.1016/j.tibs.2008.11.004
- Bröcker, C., Engelbrecht-Vandré, S. and Ungermann, C. (2010). Multisubunit tethering complexes and their role in membrane fusion. *Curr. Biol.* **20**, 943–952. doi:10.1016/j.cub.2010.09.015
- Brosseau, J.-P., Lucier, J.-F., Lapointe, E., Durand, M., Gendron, D., Gervais-Bird, J., Tremblay, K., Perreault, J.-P. and Elela, S. A. (2010). High-

- throughput quantification of splicing isoforms. *RNA* **16**, 442–449. doi:10.1261/rna.1877010
- Bryant, D., Liu, Y., Datta, S., Hariri, H., Seda, M., Anderson, G., Peskett, E., Demetriou, C., Sousa, S., Jenkins, D. et al. (2018). SNX14 mutations affect endoplasmic reticulum-associated neutral lipid metabolism in autosomal recessive spinocerebellar ataxia 20. *Hum. Mol. Genet.* **27**, 1927–1940. doi:10.1093/hmg/ddy101
- Castro, I. G., Shortill, S. P., Dziurdzik, S. K., Cadou, A., Ganesan, S., Fenech, E. J., Meyer, H., Fadel, A., David, Y., Davey, M. et al. (2021). Systematic analysis of membrane contact sites in *Saccharomyces cerevisiae* uncovers modulators of cellular lipid distribution. *bioRxiv* 2021.10.17.464712. doi:10.1101/2021.10.17.464712
- Chandra, M., Chin, Y. K.-Y., Mas, C., Feathers, J. R., Paul, B., Datta, S., Chen, K.-E., Jia, X., Yang, Z., Norwood, S. J. et al. (2019). Classification of the human phox homology (PX) domains based on their phosphoinositide binding specificities. *Nat. Commun.* **10**, 1528. doi:10.1038/s41467-019-09355-y
- Chi, R. J., Harrison, M. S. and Burd, C. G. (2015). Biogenesis of endosome-derived transport carriers. *Cell. Mol. Life Sci.* **72**, 3441–3455. doi:10.1007/s00018-015-1935-x
- Conte, A., Cuomo, A., di Fiore, P. P., Confalonieri, S., Nappo, G., Polo, S., Raimondi, A., Verhoef, L. G. G. C., Bonora, M., Tacchetti, C. et al. (2017). Reticulon 3-dependent ER-PM contact sites control EGFR nonclathrin endocytosis. *Science* **356**, 617–624. doi:10.1126/science.aah6152
- Cornick, S., Kumar, M., Moreau, F., Gaisano, H. and Chadee, K. (2019). VAMP8-mediated MUC2 mucin exocytosis from colonic goblet cells maintains innate intestinal homeostasis. *Nat. Commun.* **10**, 4306. doi:10.1038/s41467-019-11811-8
- Cui, Y., Carosi, J. M., Yang, Z., Ariotti, N., Kerr, M. C., Parton, R. G., Sargeant, T. J. and Teasdale, R. D. (2019). Retromer has a selective function in cargo sorting via endosome transport carriers. *J. Cell Biol.* **218**, 615–631. doi:10.1083/jcb.201806153
- Cullen, P. J. (2008). Endosomal sorting and signalling: an emerging role for sorting nexins. *Nat. Rev. Mol. Cell Biol.* **9**, 574–582. doi:10.1038/nrm2427
- Datta, S., Liu, Y., Hariri, H., Bowerman, J. and Henne, W. M. (2019). Cerebellar ataxia disease-associated Snx14 promotes lipid droplet growth at ER-droplet contacts. *J. Cell Biol.* **218**, 1335–1351. doi:10.1083/jcb.201808133
- Datta, S., Bowerman, J., Hariri, H., Ugrankar, R., Eckert, K. M., Corley, C., Vale, G., McDonald, J. G. and Mike Henne, W. (2020). Snx14 proximity labeling reveals a role in saturated fatty acid metabolism and ER homeostasis defective in SCAR20 disease. *Proc. Natl. Acad. Sci. USA* **117**, 33282–33294. doi:10.1073/pnas.2011124117
- Del Olmo, T., Lauzier, A., Normandin, C., Larcher, R., Lecours, M., Jean, D., Lessard, L., Steinberg, F., Boisvert, F. M. and Jean, S. (2019a). APEX2-mediated RAB proximity labeling identifies a role for RAB21 in clathrin-independent cargo sorting. *EMBO Rep.* **20**, e47192. doi:10.15252/embr.201847192
- Del Olmo, T., Lacarri re-Keita, C., Normandin, C., Jean, D., Boisvert, F.-M. and Jean, S. (2019b). RAB21 interacts with TMED10 and modulates its localization and abundance. *Biology Open* **8**, bio045336. doi:10.1242/bio.045336
- Devorkin, L. and Gorski, S. M. (2014). Monitoring autophagic flux using ref(2)P, the *Drosophila* p62 ortholog. *Cold Spring Harb. Protoc.* **2014**, 959–966. doi:10.1101/pdb.prot080333
- Diaz-Vera, J., Palmer, S., Hernandez-Ferna ndez, J. R., Dornier, E., Mitchell, L. E., Macpherson, I., Edwards, J., Zanivan, S. and Norman, J. C. (2017). A proteomic approach to identify endosomal cargoes controlling cancer invasiveness. *J. Cell Sci.* **130**, 697–711.
- Doherty, J. and Baehrecke, E. H. (2018). Life, death and autophagy. *Nat. Cell Biol.* **20**, 1110–1117. doi:10.1038/s41556-018-0201-5
- El-Brolosy, M. A. and Stainier, D. Y. R. (2017). Genetic compensation: a phenomenon in search of mechanisms. *PLoS Genet.* **13**, 1–17. doi:10.1371/journal.pgen.1006780
- Fujita, N., Huang, W., Lin, T.-H., Groulx, J.-F., Jean, S., Nguyen, J., Kuchitsu, Y., Koyama-Honda, I., Mizushima, N., Fukuda, M. et al. (2017). Genetic screen in *Drosophila* muscle identifies autophagy-mediated T-tubule remodeling and a Rab2 role in autophagy. *eLife* **6**, e23367. doi:10.7554/eLife.23367
- Gatica, D., Lahiri, V. and Klionsky, D. J. (2018). Cargo recognition and degradation by selective autophagy. *Nat. Cell Biol.* **20**, 233–242. doi:10.1038/s41556-018-0037-z
- Hao, X., Wang, Y., Ren, F., Zhu, S., Ren, Y., Jia, B., Li, Y.-P., Shi, Y. and Chang, Z. (2011). SNX25 regulates TGF- β signaling by enhancing the receptor degradation. *Cell. Signal.* **23**, 935–946. doi:10.1016/j.cellsig.2011.01.022
- Harder, L. M., Bunkborg, J. and Andersen, J. S. (2014). Inducing autophagy: a comparative phosphoproteomic study of the cellular response to ammonia and rapamycin. *Autophagy* **10**, 339–355. doi:10.4161/auto.26863
- Hariri, H., Rogers, S., Ugrankar, R., Liu, Y. L., Feathers, J. R. and Henne, W. M. (2018). Lipid droplet biogenesis is spatially coordinated at ER–vacuole contacts under nutritional stress. *EMBO Rep.* **19**, 57–72. doi:10.15252/embr.201744815
- Hariri, H., Speer, N., Bowerman, J., Rogers, S., Fu, G., Reetz, E., Datta, S., Feathers, J. R., Ugrankar, R., Nicastro, D. et al. (2019). Mdm1 maintains endoplasmic reticulum homeostasis by spatially regulating lipid droplet biogenesis. *J. Cell Biol.* **218**, 1319–1334. doi:10.1083/jcb.201808119
- Heged s, K., Tak ts, S., Boda, A., Jipa, A., Nagy, P., Varga, K., Kov cs, A. L. and Juh sz, G. (2016). The Ccz1-Mon1-Rab7 module and Rab5 control distinct steps of autophagy. *Mol. Biol. Cell* **27**, 3132–3142. doi:10.1091/mbc.e16-03-0205
- Henne, W. M., Zhu, L., Balogi, Z., Stefan, C., Pleiss, J. A. and Emr, S. D. (2015). Mdm1/Snx13 is a novel ER-endolysosomal interorganelle tethering protein. *J. Cell Biol.* **210**, 541–551. doi:10.1083/jcb.201503088
- Hong, W. (2005). SNAREs and traffic. *Biochim. Biophys. Acta* **1744**, 120–144. doi:10.1016/j.bbamcr.2005.03.014
- Itakura, E., Kishi-Itakura, C. and Mizushima, N. (2012). The Hairpin-type Tail-Anchored SNARE Syntaxin 17 Targets to Autophagosomes for Fusion with Endosomes/Lysosomes. *Cell* **151**, 1256–1269. doi:10.1016/j.cell.2012.11.001
- Jean, S. and Kiger, A. A. (2012). Coordination between RAB GTPase and phosphoinositide regulation and functions. *Nat. Rev. Mol. Cell Biol.* **13**, 463–470. doi:10.1038/nrm3379
- Jean, S. and Kiger, A. A. (2016). VAMP8-3xHA uptake assay in HeLa cells. *Bio. Protoc.* **6**, e1739. doi:10.21769/BioProtoc.1739
- Jean, S., Cox, S., Nassari, S. and Kiger, A. A. (2015). Starvation-induced MTMR13 and RAB21 activity regulates VAMP8 to promote autophagosome-lysosome fusion. *EMBO Rep.* **16**, 297–311. doi:10.15252/embr.201439464
- Jiang, P., Nishimura, T., Sakamaki, Y., Itakura, E., Hatta, T., Natsume, T. and Mizushima, N. (2014). The HOPS complex mediates autophagosome-lysosome fusion through interaction with syntaxin 17. *Mol. Biol. Cell* **25**, 1327–1337. doi:10.1091/mbc.e13-08-0447
- Knaevelsrud, H., S r ng, K., Raiborg, C., H berg, K., Rasmussen, F., Brech, A., Liest l, K., Rusten, T. E., Stenmark, H., Neufeld, T. P. et al. (2013). Membrane remodeling by the PX-BAR protein SNX18 promotes autophagosome formation. *J. Cell Biol.* **202**, 331–349. doi:10.1083/jcb.201205129
- Koga, H., Kaushik, S. and Cuervo, A. M. (2010). Altered lipid content inhibits autophagic vesicular fusion. *FASEB J* **24**, 3052–3065. doi:10.1096/fj.09-144519
- Korolchuk, V. I., Saiki, S., Lichtenberg, M., Siddiqui, F. H., Roberts, E. A., Imarisio, S., Jahreis, L., Sarkar, S., Futter, M., Menzies, F. M. et al. (2011). Lysosomal positioning coordinates cellular nutrient responses. *Nat. Cell Biol.* **13**, 453–462. doi:10.1038/ncb2204
- Kriegenburg, F., Ungermann, C. and Reggiori, F. (2018). Coordination of autophagosome–lysosome fusion by Atg8 family members. *Curr. Biol.* **28**, R512–R518. doi:10.1016/j.cub.2018.02.034
- Kuchitsu, Y., Homma, Y., Fujita, N. and Fukuda, M. (2018). Rab7 knockout unveils regulated autolysosome maturation induced by glutamine starvation. *J. Cell Sci.* **131**, jcs215442. doi:10.1242/jcs.215442
- Lamb, C. A., Yoshimori, T. and Tooze, S. A. (2013). The autophagosome: origins unknown, biogenesis complex. *Nat. Rev. Mol. Cell Biol.* **14**, 759–774. doi:10.1038/nrm3696
- Levine, B. and Kroemer, G. (2019). Biological functions of autophagy genes: a disease perspective. *Cell* **176**, 11–42. doi:10.1016/j.cell.2018.09.048
- Livak, K. J. and Schmittgen, T. D. (2001). Analysis of relative gene expression data using real-time quantitative PCR and the 2 $^{-\Delta\Delta CT}$ method. *Methods* **25**, 402–408. doi:10.1006/meth.2001.1262
- L rincz, P. and Juh sz, G. (2019). Autophagosome-lysosome fusion. *J. Mol. Biol.* **432**, 2462–2482. doi:10.1016/j.jmb.2019.10.028
- L rincz, P., Mauvezin, C. and Juh sz, G. (2017a). Exploring Autophagy in *Drosophila*. *Cells* **6**, 22. doi:10.3390/cells6030022
- L rincz, P., T th, S., Benk , P., Lakatos, Z., Boda, A., Glatz, G., Zobel, M., Bisi, S., Heged s, K., Tak ts, S. et al. (2017b). Rab2 promotes autophagic and endocytic lysosomal degradation. *J. Cell Biol.* **216**, 1937–1947. doi:10.1083/jcb.201611027
- Ma, M., Kumar, S., Purushothaman, L., Babst, M., Ungermann, C., Chi, R. J. and Burd, C. G. (2018). Lipid trafficking by yeast Snx4 family SNX-BAR proteins promotes autophagy and vacuole membrane fusion. *Mol. Biol. Cell* **29**, 2190–2200. doi:10.1091/mbc.E17-12-0743
- Maruzs, T., L rincz, P., Szatm ri, Z., Sz plaki, S., S ndor, Z., Lakatos, Z., Puska, G., Juh sz, G. and Sass, M. (2015). Retromer ensures the degradation of autophagic cargo by maintaining lysosome function in *Drosophila*. *Traffic* **16**, 1088–1107. doi:10.1111/tra.12309
- Mas, C., Norwood, S. J., Bugarcic, A., Kinna, G., Leneva, N., Kovtun, O., Ghai, R., Ona Yanez, L. E., Davis, J. L., Teasdale, R. D. et al. (2014). Structural basis for different phosphoinositide specificities of the PX domains of sorting nexins regulating G-protein signaling. *J. Biol. Chem.* **289**, 28554–28568. doi:10.1074/jbc.M114.595959
- Matsui, T., Jiang, P., Nakano, S., Sakamaki, Y., Yamamoto, H. and Mizushima, N. (2018). Autophagosomal YKT6 is required for fusion with lysosomes independently of syntaxin 17. *J. Cell Biol.* **217**, 2633–2645. doi:10.1083/jcb.201712058
- Mauvezin, C., Ayala, C., Braden, C. R., Kim, J. and Neufeld, T. P. (2014). Assays to monitor autophagy in *Drosophila*. *Methods (San Diego, Calif)* **68**, 134–139. doi:10.1016/j.ymeth.2014.03.014
- Mauvezin, C., Neisch, A. L., Ayala, C. I., Kim, J., Beltrame, A., Braden, C. R., Gardner, M. K., Hays, T. S. and Neufeld, T. P. (2016). Coordination of autophagosome–lysosome fusion and transport by a Klp98A–Rab14 complex in *Drosophila*. *J. Cell Sci.* **129**, 971–982. doi:10.1242/jcs.175224

- Miller, S. E., Sahlender, D. A., Graham, S. C., Höning, S., Robinson, M. S., Peden, A. A. and Owen, D. J. (2011). The molecular basis for the endocytosis of small R-SNAREs by the clathrin adaptor CALM. *Cell* **147**, 1118–1131. doi:10.1016/j.cell.2011.10.038
- Miyagawa, K., Oe, S., Honma, Y., Izumi, H., Baba, R. and Harada, M. (2016). Lipid-Induced Endoplasmic Reticulum Stress Impairs Selective Autophagy at the Step of Autophagosome-Lysosome Fusion in Hepatocytes. *Am. J. Pathol.* **186**, 1861–1873. doi:10.1016/j.ajpath.2016.03.003
- Mizushima, N., Levine, B., Cuervo, A. M. and Klionsky, D. J. (2008). Autophagy fights disease through cellular self-digestion. *Nature* **451**, 1069–1075. doi:10.1038/nature06639
- Mizushima, N., Yoshimori, T. and Ohsumi, Y. (2011). The role of Atg proteins in autophagosome formation. *Annu. Rev. Cell Dev. Biol.* **27**, 107–132. doi:10.1146/annurev-cellbio-092910-154005
- Moreau, K., Ravikumar, B., Renna, M., Puri, C. and Rubinsztein, D. C. (2011). Autophagosome precursor maturation requires homotypic fusion. *Cell* **146**, 303–317. doi:10.1016/j.cell.2011.06.023
- Moreau, K., Fleming, A., Imarisio, S., Ramirez, A. L., Mercer, J. L., Jimenez-Sanchez, M., Bento, C. F., Puri, C., Zavodszky, E., Siddiqi, F. et al. (2014). PICALM modulates autophagy activity and tau accumulation. *Nat. Commun.* **5**, 1–19. doi:10.1038/ncomms5998
- Moretti, F., Bergman, P., Dodgson, S., Marcellin, D., Claerr, I., Goodwin, J. M., DeJesus, R., Kang, Z., Antczak, C., Begue, D. et al. (2018). TMEM41B is a novel regulator of autophagy and lipid mobilization. *EMBO Rep.* **19**, e45889. doi:10.15252/embr.201845889
- Morita, K., Hama, Y., Izume, T., Tamura, N., Ueno, T., Yamashita, Y., Sakamaki, Y., Mimura, K., Morishita, H., Shihoya, W. et al. (2018). Genome-wide CRISPR screen identifies TMEM41B as a gene required for autophagosome formation. *J. Cell Biol.* **217**, 3817–3828. doi:10.1083/jcb.201804132
- Nair, U., Jotwani, A., Geng, J., Gammoh, N., Richerson, D., Yen, W.-L., Griffith, J., Nag, S., Wang, K., Moss, T. et al. (2011). SNARE proteins are required for macroautophagy. *Cell* **146**, 290–302. doi:10.1016/j.cell.2011.06.022
- Nair-Gupta, P., Baccarini, A., Tung, N., Seyffer, F., Florey, O., Huang, Y., Banerjee, M., Overholtzer, M., Roche, P. A., Tampé, R. et al. (2014). TLR signals induce phagosomal MHC-I delivery from the endosomal recycling compartment to allow cross-presentation. *Cell* **158**, 506–521. doi:10.1016/j.cell.2014.04.054
- Nakamura, S. and Yoshimori, T. (2017). New insights into autophagosome-lysosome fusion. *J. Cell Sci.* **130**, 1209–1216. doi:10.1242/jcs.196352
- Nguyen, T. B., Louie, S. M., Daniele, J. R., Zoncu, R., Nomura, D. K., Olzmann, J. A., Nguyen, T. B., Louie, S. M., Daniele, J. R., Tran, Q. et al. (2017). DGAT1-dependent lipid droplet biogenesis protects mitochondrial function during starvation-induced autophagy. *Dev. Cell* **42**, 9–21.e5. doi:10.1016/j.devcel.2017.06.003
- Numrich, J. and Ungermann, C. (2014). Endocytic Rabs in membrane trafficking and signaling. *Biol. Chem.* **395**, 327–333. doi:10.1515/hsz-2013-0258
- Okayama, M., Arakawa, T., Tanimura, A., Mizoguchi, I., Tajima, Y., Takuma, T., Mizoguchi, I., Arakawa, T., Okayama, M. and Takuma, T. (2009). Role of VAMP8/endobrevin in constitutive exocytotic pathway in HeLa cells. *Cell Struct. Funct.* **34**, 115–125. doi:10.1247/csf.09013
- Patel, D. and Witt, S. N. (2017). Ethanolamine and Phosphatidylethanolamine: Partners in Health and Disease. *Oxid. Med. Cell. Longevity* **2017**, 4829180. doi:10.1155/2017/4829180
- Pattu, V., Qu, B., Marshall, M., Becherer, U., Junker, C., Matti, U., Schwarz, E. C., Krause, E., Hoth, M. and Rettig, J. (2011). Syntaxin7 is required for lytic granule release from cytotoxic T lymphocytes. *Traffic* **12**, 890–901. doi:10.1111/j.1600-0854.2011.01193.x
- Rambold, A. S., Cohen, S. and Lippincott-Schwartz, J. (2015). Fatty acid trafficking in starved cells: regulation by lipid droplet lipolysis, autophagy, and mitochondrial fusion dynamics. *Dev. Cell* **32**, 678–692. doi:10.1016/j.devcel.2015.01.029
- Ravussin, A., Brech, A., Tooze, S. A. and Stenmark, H. (2021). The phosphatidylinositol 3-phosphate-binding protein SNX4 controls ATG9A recycling and autophagy. *J. Cell Sci.* **134**, jcs250670. doi:10.1242/jcs.250670
- Reekmans, S. M., Pflanzner, T., Gordts, P. L. S. M., Isbert, S., Zimmermann, P., Annaert, W., Weggen, S., Roebroek, A. J. M. and Pietrzik, C. U. (2010). Inactivation of the proximal NPXY motif impairs early steps in LRP1 biosynthesis. *Cell. Mol. Life Sci.* **67**, 135–145. doi:10.1007/s00018-009-0171-7
- Reggiori, F. and Ungermann, C. (2017). Autophagosome maturation and fusion. *J. Mol. Biol.* **429**, 486–496. doi:10.1016/j.jmb.2017.01.002
- Renard, H.-F., Garcia-Castillo, M. D., Chambon, V., Lamaze, C. and Johannes, L. (2015). Shiga toxin stimulates clathrin-independent endocytosis of the VAMP2, VAMP3 and VAMP8 SNARE proteins. *J. Cell Sci.* **128**, 2891–2902. doi:10.1242/jcs.171116
- Rusten, T. E., Lindmo, K., Juhász, G., Sass, M., Seglen, P. O., Brech, A. and Stenmark, H. (2004). Programmed autophagy in the Drosophila fat body is induced by ecdysone through regulation of the PI3K pathway. *Dev. Cell* **7**, 179–192. doi:10.1016/j.devcel.2004.07.005
- Saric, A., Freeman, S. A., Williamson, C. D., Jarnik, M., Guardia, C. M., Fernandopulle, M. S., Gershlick, D. C. and Bonifacio, J. S. (2021). SNX19 restricts endolysosome motility through contacts with the endoplasmic reticulum. *Nat. Commun.* **12**, 4552. doi:10.1038/s41467-021-24709-1
- Scott, R. C., Schuldiner, O. and Neufeld, T. P. (2004). Role and regulation of starvation-induced autophagy in the Drosophila fat body. *Dev. Cell* **7**, 167–178. doi:10.1016/j.devcel.2004.07.009
- Søreng, K., Munson, M. J., Lamb, C. A., Bjørndal, G. T., Pankiv, S., Carlsson, S. R., Tooze, S. A. and Simonsen, A. (2018). SNX18 regulates ATG9A trafficking from recycling endosomes by recruiting Dynamin-2. *EMBO Rep.* **19**, e44837. doi:10.15252/embr.201744837
- Suh, J. M., Stenesen, D., Peters, J. M., Inoue, A., Cade, A. and Graff, J. M. (2008). An RGS-containing sorting Nexin controls Drosophila lifespan. *PLoS ONE* **3**, e2152. doi:10.1371/journal.pone.0002152
- Sullender, M., Hegde, M., Vaimberg, E. W., Donovan, K. F., Smith, I., Tothova, Z., Wilen, C., Orchard, R., Virgin, H. W., Doench, J. G. et al. (2016). Optimized sgRNA design to maximize activity and minimize off-target effects of crispr-cas9. *Nat. Biotechnol.* **34**, 184–191. doi:10.1038/nbt.3437
- Takáts, S., Nagy, P., Varga, A., Pircs, K., Kárpáti, M., Varga, K., Kovács, A. L., Hegedűs, K. and Juhász, G. (2013). Autophagosomal Syntaxin17-dependent lysosomal degradation maintains neuronal function in Drosophila. *J. Cell Biol.* **201**, 531–539. doi:10.1083/jcb.201211160
- Takáts, S., Pircs, K., Nagy, P., Varga, A., Karpáti, M., Hegedűs, K., Kramer, H., Kovács, A. L., Sass, M. and Juhász, G. (2014). Interaction of the HOPS complex with Syntaxin 17 mediates autophagosome clearance in Drosophila. *Mol. Biol. Cell* **25**, 1338–1354. doi:10.1091/mbc.e13-08-0449
- Takáts, S., Glatz, G., Szenci, G., Boda, A., Horváth, G. V., Hegedűs, K., Kovács, A. L. and Juhász, G. (2018). Non-canonical role of the SNARE protein Ykt6 in autophagosome-lysosome fusion. *PLoS Genet.* **14**, 1–23. doi:10.1371/journal.pgen.1007359
- Tan, X., Sun, Y., Thapa, N., Liao, Y., Hedman, A. C. and Anderson, R. A. (2015). EGFR signaling, lysosomal sorting, and degradation. *EMBO J.* **34**, 475–490. doi:10.15252/embj.201489425
- Torng, T. and Wickner, W. (2021). Phosphatidylinositol and phosphatidylinositol-3-phosphate activate HOPS to catalyze SNARE assembly, allowing small headgroup lipids to support the terminal steps of membrane fusion. *Mol. Biol. Cell* **32**, ar19. doi:10.1091/mbc.E21-07-0373
- Ugrankar, R., Bowerman, J., Hariri, H., Chandra, M., Chen, K., Bossanyi, M.-F., Datta, S., Rogers, S., Eckert, K. M., Vale, G. et al. (2019). Drosophila Snazarus regulates a lipid droplet population at plasma membrane-droplet contacts in adipocytes. *Dev. Cell* **50**, 557–572.e5. doi:10.1016/j.devcel.2019.07.021
- van Weering, J. R. T. and Cullen, P. J. (2014). Membrane-associated cargo recycling by tubule-based endosomal sorting. *Semin. Cell Dev. Biol.* **31**, 40–47. doi:10.1016/j.semcdb.2014.03.015
- Velázquez, A. P., Tatsuta, T., Ghillebert, R., Drescher, I. and Graef, M. (2016). Lipid droplet-mediated ER homeostasis regulates autophagy and cell survival during starvation. *J. Cell Biol.* **212**, 621–631. doi:10.1083/jcb.201508102
- Wang, Z., Miao, G., Xue, X., Guo, X., Yuan, C., Wang, Z., Zhang, G., Chen, Y., Feng, D., Hu, J. et al. (2016). The Vici syndrome protein EPG5 is a Rab7 effector that determines the fusion specificity of autophagosomes with late endosomes/lysosomes. *Mol. Cell* **63**, 781–795. doi:10.1016/j.molcel.2016.08.021
- Wijdeven, R. H., Janssen, H., Nahidiazar, L., Janssen, L., Jalink, K., Berlin, I. and Neefjes, J. (2016). Cholesterol and ORP1L-mediated ER contact sites control autophagosome transport and fusion with the endocytic pathway. *Nat. Commun.* **7**, 11808. doi:10.1038/ncomms11808
- Zhu, D., Zhang, Y., Lam, P. P. L., Dolai, S., Liu, Y., Cai, E. P., Choi, D., Schroer, S. A., Kang, Y., Allister, E. M. et al. (2012). Dual role of VAMP8 in regulating insulin exocytosis and islet β cell growth. *Cell Metab.* **16**, 238–249. doi:10.1016/j.cmet.2012.07.001

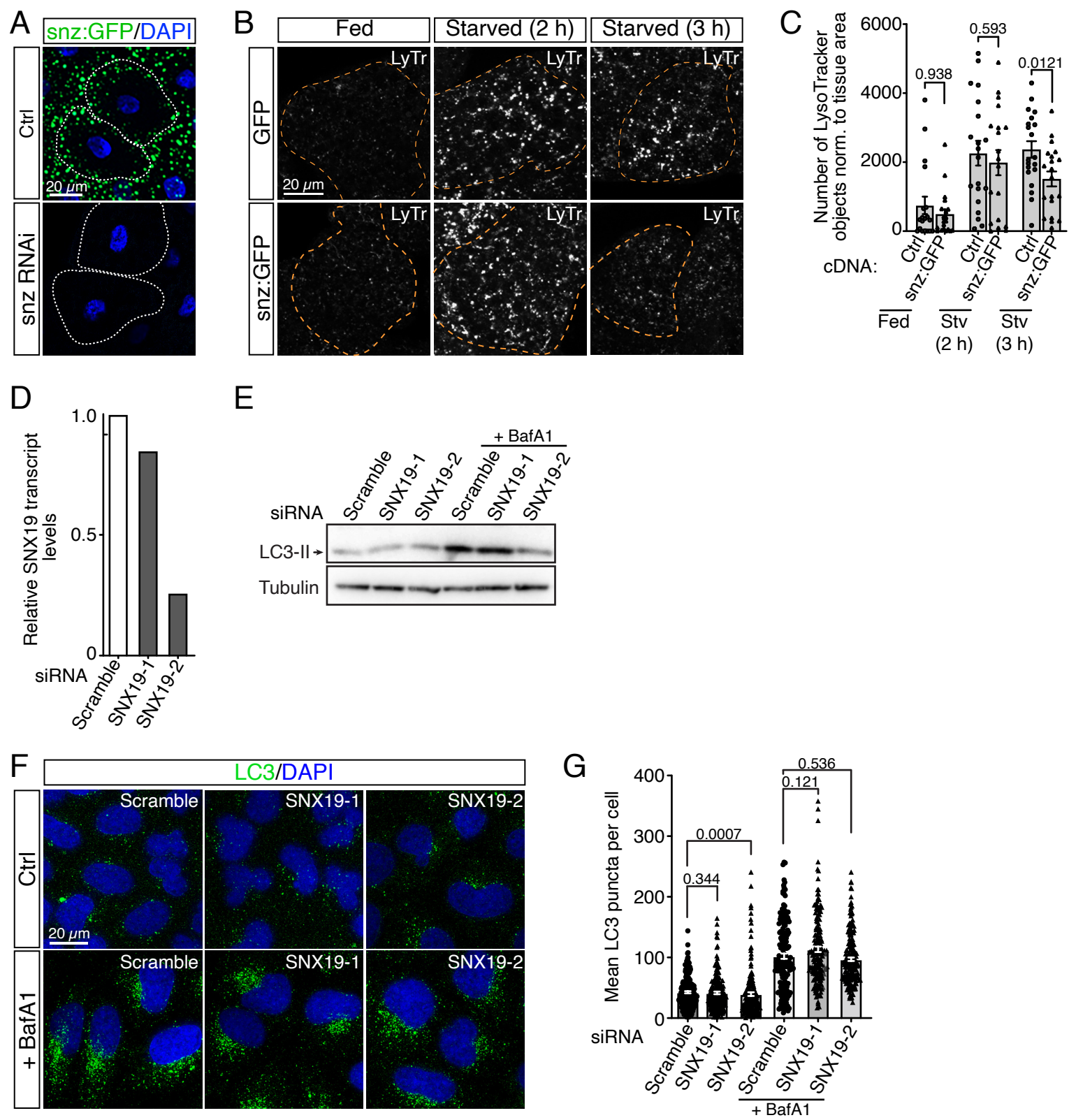


Fig. S1. SNX19 loss does not affect autophagy (A) Snz:GFP-expressing flies in the presence and absence of snz RNAi. Images are representative of three independent experiments. (B) Representative images of LyTr-stained fed and starved fat bodies overexpressing snz:GFP. (C). Mean LyTr objects normalized to the tissue area. Bars represent the mean, individual points represent single fat body values, and the error bars are the SEM ($n=4$ independent experiments). (D) qRT-PCR validation of SNX19 siRNA efficiencies. Reactions were normalized to control, which were set at 1. (E) Anti-LC3 western blots of SNX19 siRNA-transfected HeLa cells grown in full DMEM treated with or without bafilomycin A1. Tubulin was used as a loading control. $n=3$ independent experiments (F) Immunofluorescence analysis of endogenous LC3 (green) in scramble or SNX19 siRNA-transfected HeLa cells grown in full DMEM with or without bafilomycin A1 (BafA1) treatment. Nuclei were counterstained with 4',6-diamidino-2-phenylindole (DAPI). Images are representative of three independent experiments. (G) Quantification of LC3 puncta per cell. Bars represent the mean, individual points or triangles represent single-cell values, and the error bars are the SEM ($n=3$ independent experiments).

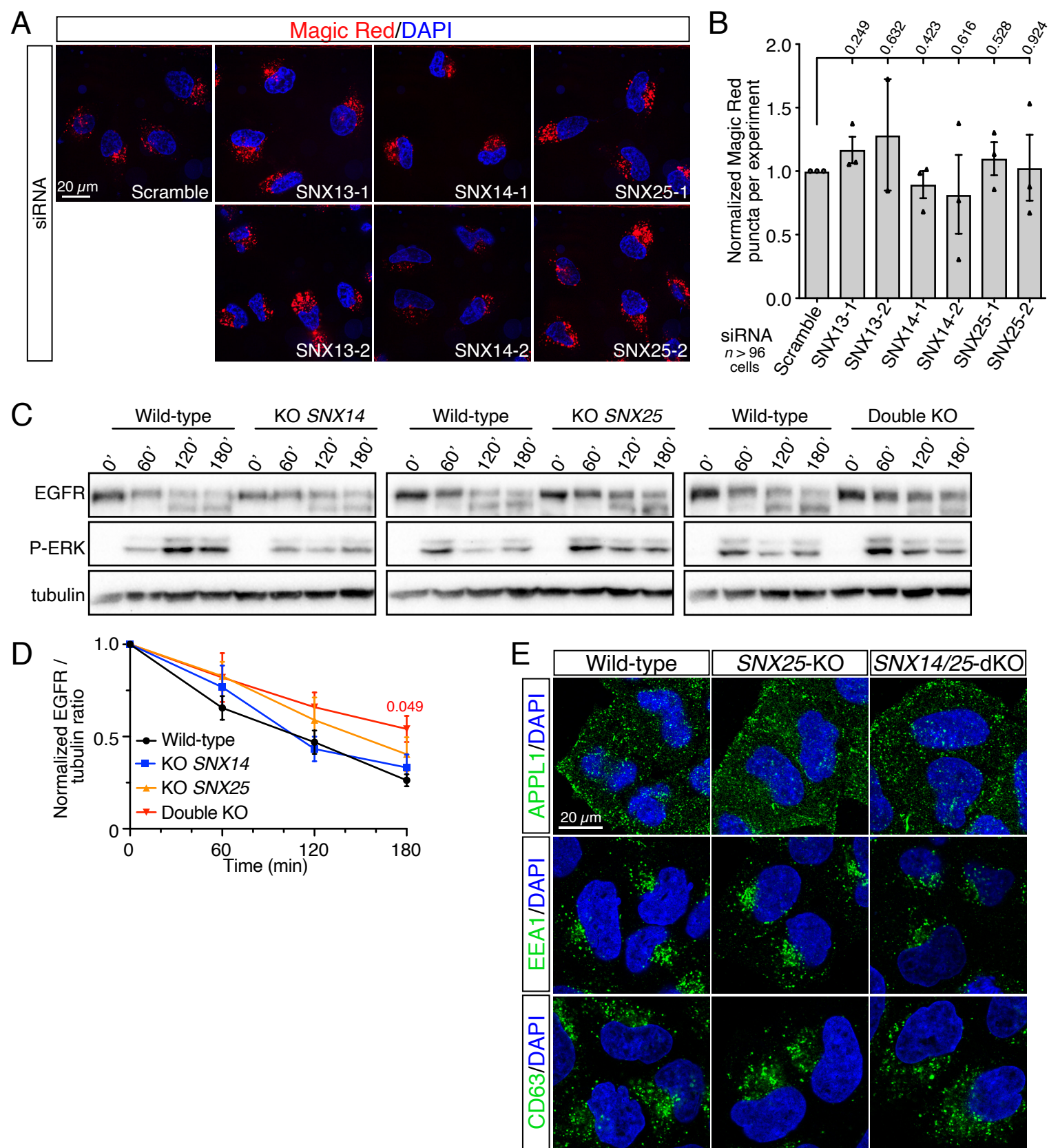


Fig. S2. *SNX14* and *SNX25* loss modestly impairs lysosomal functions (A) Representative images of Magic Red staining to detect cathepsin B activity in HeLa cells transfected with siRNAs against SNX13, SNX14, and SNX25. (B) Quantification of the normalized number of Magic Red puncta per experiment. Bars represent the mean, individual points or triangles represent single experimental values, and the error bars are the SEM ($n=3$ independent experiments). (C) Effects of *SNX14*, *SNX25*, and *SNX14/SNX25* KO on EGFR activation and degradation after stimulation with 100 nM EGF. (D) Normalized integrated density ratios of EGFR to tubulin in the various HeLa KO populations. Error bars are the SEM ($n=3$ independent experiments). (E) Representative immunofluorescent images of *SNX25* KO and *SNX14/SNX25* double KO cells stained for APPL1, EEA1, and CD63 and counterstained with DAPI.

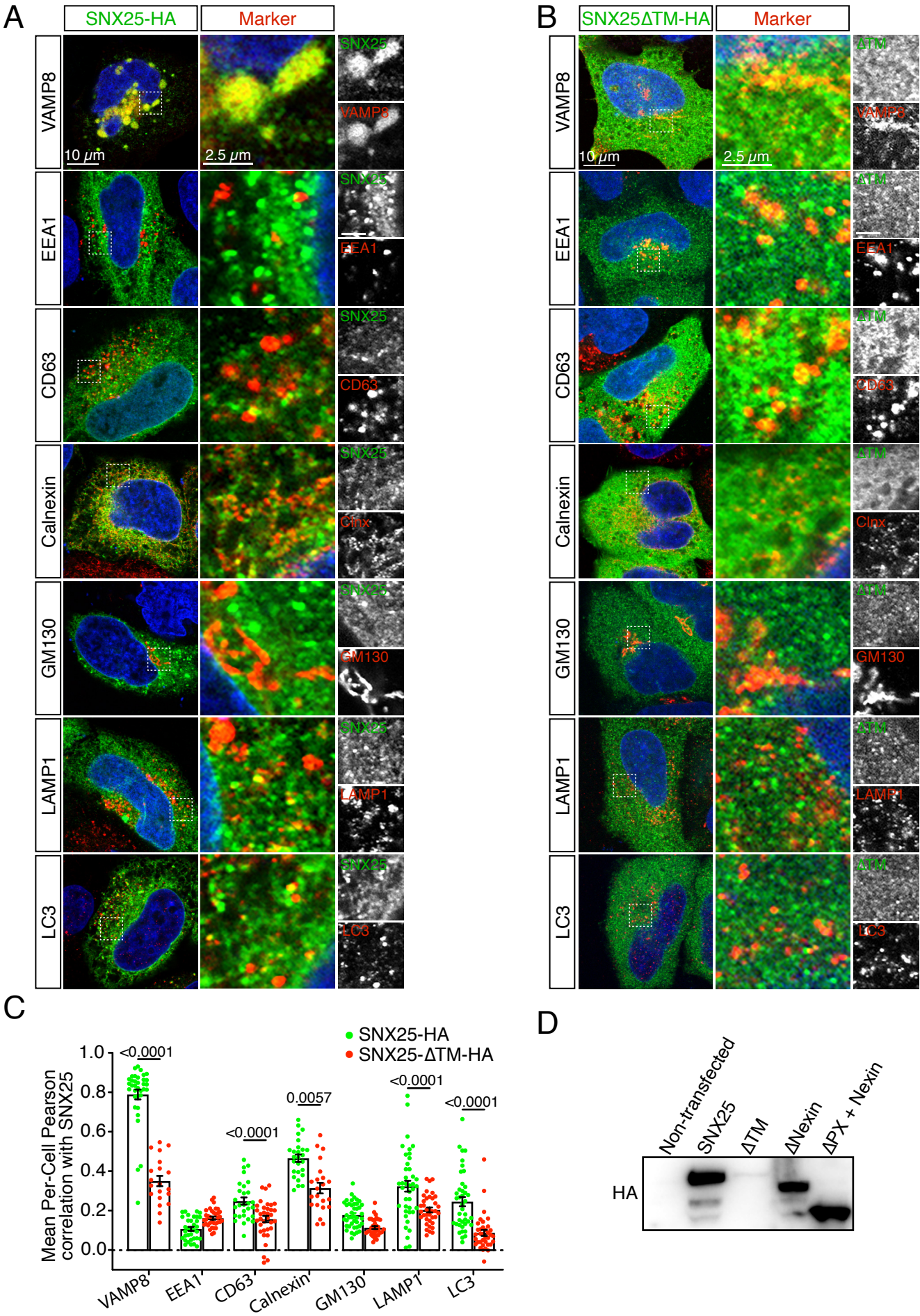


Fig. S3. SNX25 strongly colocalizes with VAMP8 and to some degree with other cellular compartments (A and B) Representative immunofluorescent images of cells transfected with (A) full-length SNX25-HA and (B) SNX25- Δ TM-HA, which lacks the TM domains. Cells were either co-transfected with VAMP8-GFP or immunostained for EEA1, CD63, calnexin, GM130, LAMP1, or LC3. (C) Per-cell Pearson's correlations between SNX25-HA/SNX25- Δ TM-HA and the various markers. Bars represent the mean, individual points represent single-cell values, and the error bars are the SEM ($n=3$ independent experiments). (D) Anti-HA western blot of SNX25 constructs used in the KO/rescue experiments.

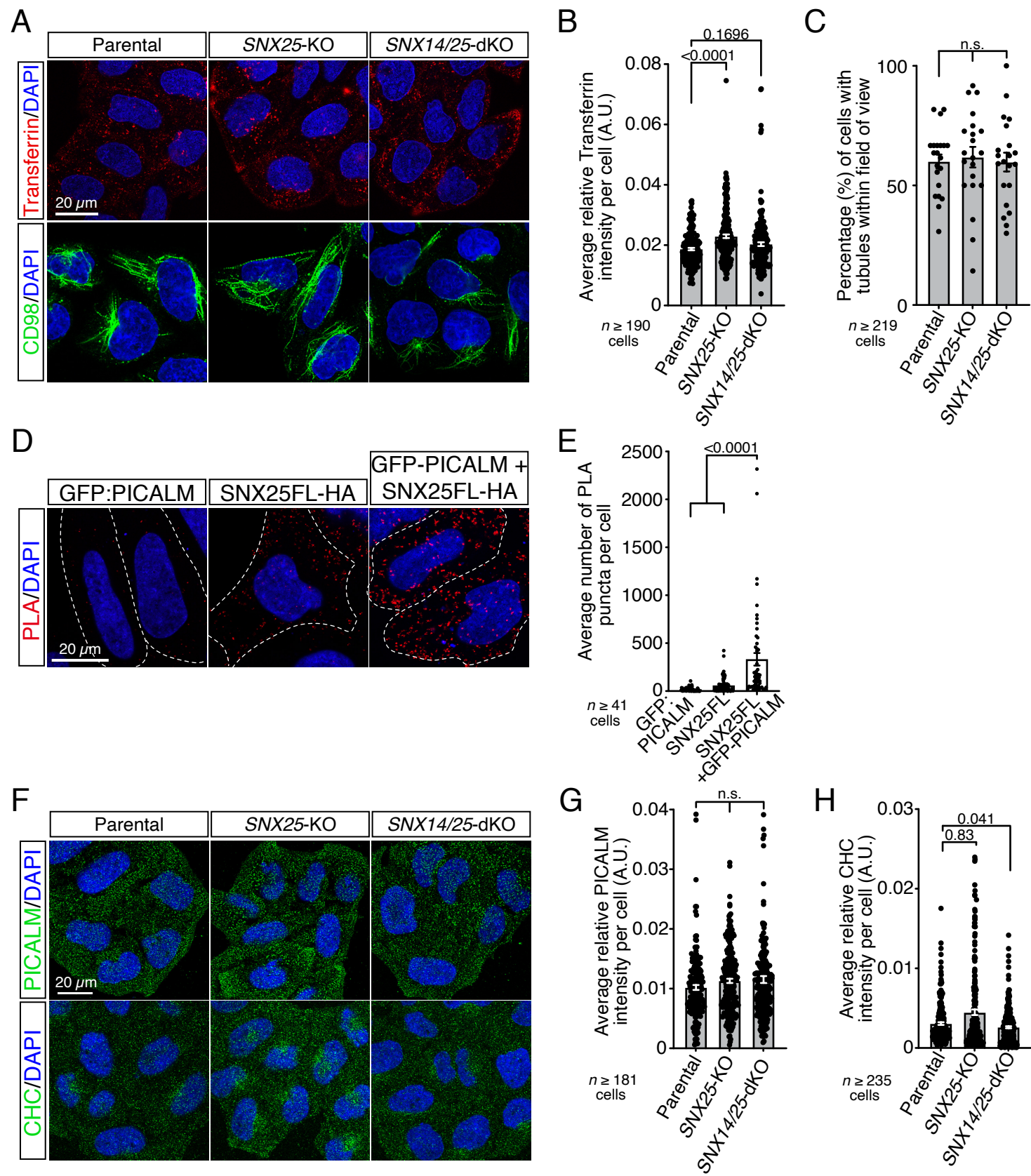


Fig. S4. *SNX25* is dispensable for clathrin-dependent and -independent endocytosis and PICALM recruitment (A) Transferrin and CD98 uptake in WT, *SNX25* KO, and *SNX14/25* double KO cells. Cells were acid-washed for both uptakes and before fixation to assess only internalized transferrin and CD98. (B and C) Average per-cell transferrin intensity (B) and percentage of cells with tubules (C). Bars represent the mean, individual points represent single-cell values, and the error bars are the SEM ($n=3$ independent experiments). (D) PLA immunofluorescence shows the respective proximities between GFP-PICALM and SNX25FL-HA. GFP-PICALM and SNX25FL-HA were also transfected individually and probed with both antibodies as PLA controls (first two panels). PLA puncta are shown in red and nuclei in blue. Dotted lines define individual cells. (E) Quantification of the PLA shown in D. Bars represent the average number of PLA puncta per cell, individual points represent single cells, and the error bars are the SEM ($n=3$ independent experiments). (F) Immunofluorescence analysis of PICALM and clathrin heavy chain (CHC) in parental and KO cells. Confocal images were acquired on the ventral side of cells to image PM-localized PICALM and CHC. (G and H) Average per-cell PICALM (G) and CHC (H) intensities. Bars represent the mean, individual points represent single-cell values, and the error bars are the SEM ($n=3$ independent experiments). A.U., arbitrary units, n.s., not significant.

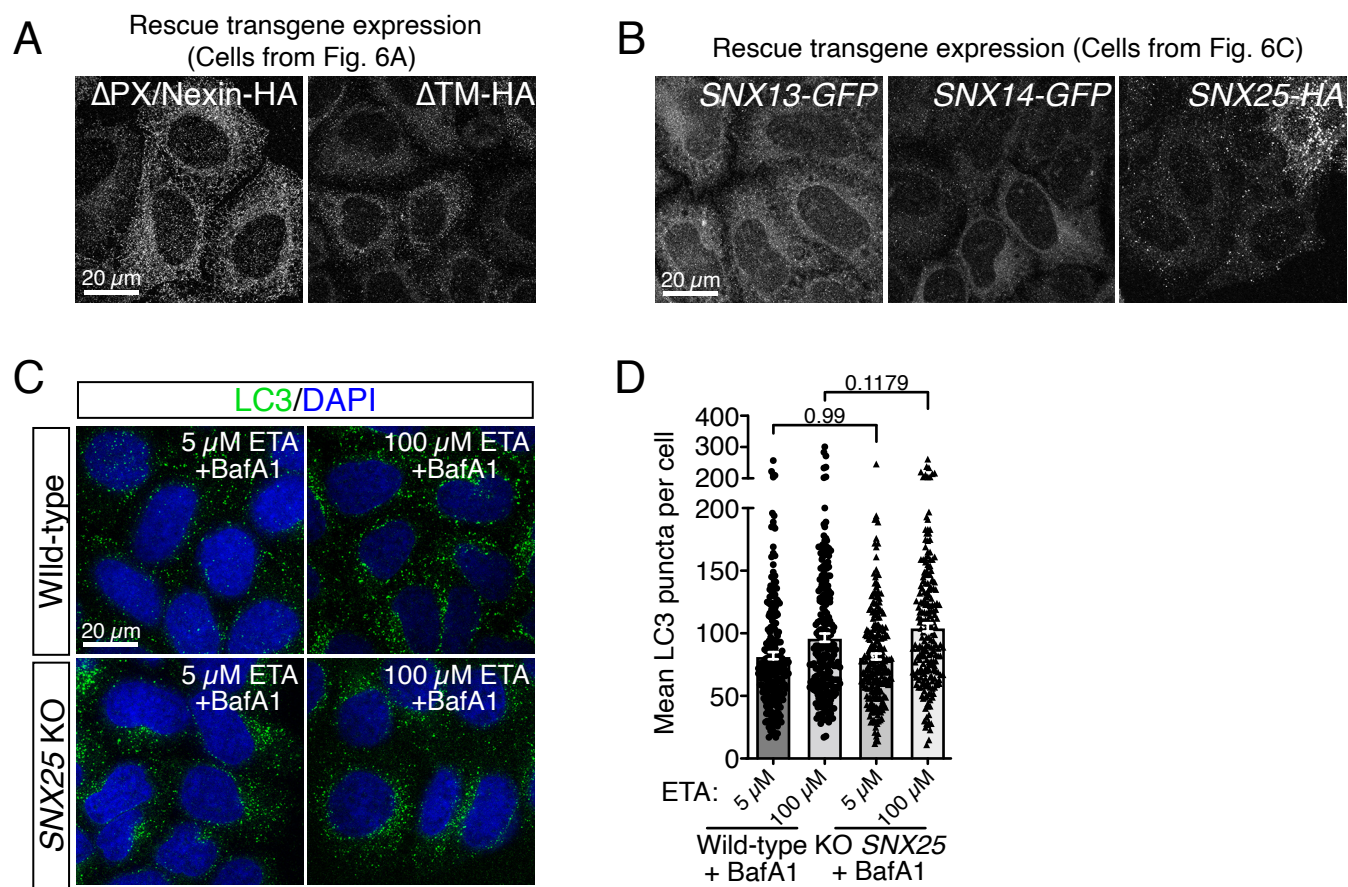


Fig. S5. Ethanolamine addition does not affect autophagosome formation (A) HA immunofluorescence of SNX25 KO cells expressing the Δ PX/ Δ Nexin-HA or Δ TM-HA mutants. (B) GFP fluorescence of SNX13-GFP or SNX14-GFP and anti-HA immunofluorescence of SNX25-HA in SNX25 KO cells. (C) Immunofluorescence analysis of endogenous LC3 (green) in parental of SNX25 KO HeLa cells grown in full DMEM with or without bafilomycin A1 (BafA1) treatment supplement with two concentrations of ETA for 24 hours prior cell fixation. Nuclei were counterstained with 4',6-diamidino-2-phenylindole (DAPI). Images are representative of three independent experiments. Parental HeLa cells were stained for LC3 in the same experimental sets to validate the BafA1 treatment (mean number of LC3 puncta per cell was 18.75 ± 0.83 (SEM)) (D) Quantification of LC3 puncta per cell. Bars represent the mean, individual points or triangles represent single-cell values, and the error bars are the SEM ($n=3$ independent experiments).

Table S1. List of primers used for ddPCR reactions

[Click here to download Table S1](#)